J. Fluid Mech. (2003), *vol.* 496, *pp.* 365–404. © 2003 Cambridge University Press
DOI: 10.1017/S0022112003006190 Printed in the United Kingdom

Time-averaged flow over a hydrofoil at high Reynolds number

By DWAYNE A. BOURGOYNE, JOSHUA M. HAMEL, STEVEN L. CECCIO AND DAVID R. DOWLING

Department of Mechanical Engineering, University of Michigan, Ann Arbor, MI 48109, USA

(Received 13 February 2003 and in revised form 26 June 2003)

At high Reynolds number, the flow of an incompressible viscous fluid over a lifting surface is a rich blend of fluid dynamic phenomena. Here, boundary layers formed at the leading edge develop over both the suction and pressure sides of the lifting surface, transition to turbulence, separate near the foil's trailing edge, combine in the near wake, and eventually form a turbulent far-field wake. The individual elements of this process have been the subject of much prior work. However, controlled experimental investigations of these flow phenomena and their interaction on a lifting surface at Reynolds numbers typical of heavy-lift aircraft wings or full-size ship propellers (chord-based Reynolds numbers, $Re_C \sim 10^7 - 10^8$) are largely unavilable. This paper presents results from an experimental effort to identify and measure the dominant features of the flow over a two-dimensional hydrofoil at nominal Re_C values from near one million to more than 50 million. The experiments were conducted in the US Navy's William B. Morgan Large Cavitation Channel with a solid-bronze hydrofoil (2.1 m chord, 3.0 m span, 17 cm maximum thickness) at flow speeds from 0.25 to 18.3 m s^{-1}. The foil section, a modified NACA 16 with a pressure side that is nearly flat and a suction side that terminates in a blunt trailing-edge bevel, approximates the cross-section of a generic naval propeller blade. Time-averaged flow-field measurements drawn from laser-Doppler velocimetry, particle-imaging velocimetry, and static pressure taps were made for two trailing-edge bevel angles (44° and 56°). These velocity and pressure measurements were concentrated in the trailing-edge and near-wake regions, but also include flow conditions upstream and far downstream of the foil, as well as static pressure distributions on the foil surface and test section walls. Observed Reynolds-number variations in the time-averaged flow over the foil are traced to changes in suction-side boundary-layer transition and separation. Observed Reynolds-number variations in the time-averaged near wake suggest significant changes occur in the dynamic flow in the range of Re_C investigated.

1. Introduction

Relative motion between a submerged body and a viscous incompressible fluid induces hydrodynamic lift and drag. The shape of the body and the characteristics of its flow field govern the distributions of surface pressure and shear stress that lead to these forces. Typically, the steady or unsteady components of these hydrodynamic forces ultimately determine the utility of the body for potential applications. Air- and water-borne transportation systems are often characterized by turbulent high-Reynolds-number flows. Thus, experimental work in this area commonly strives to deduce scaling laws and cause-and-effect relationships, while computational efforts

focus on developing and validating predictive flow models. Unfortunately, the scarcity of experimental studies at high Reynolds numbers hampers all of these approaches. The goal of this paper is to address this situation through the presentation of experimental results for the time-averaged incompressible flow over a lifting surface at Reynolds numbers approaching those of heavy-lift aircraft wings and full-scale ship propellers.

The surface-bounded near-wake and far-wake flows formed by a lifting surface are phenomenologically interesting and have practical importance. For example, surface curvature influences boundary-layer development, transition and separation, which together determine the initial conditions for the foil's wake. Given that these phenomena may all behave differently with increasing Reynolds number, any overall scaling for lift, drag, hydroacoustic noise, or other foil-performance measure may result from the interplay of multiple phenomena. On the practical side, high-Reynolds-number lifting surfaces are essential for flight, manoeuvring, propulsion and control of air- and water-borne vehicles. In such applications, the lifting surface is designed to meet performance criteria. Given the complexity of flow phenomena and the wide range of length and time scales that must be managed in high-Reynolds-number turbulence, it is safe to say that the development of the required design tools is not yet complete. For lifting surfaces in incompressible flow, this situation exists in part because of the lack of controlled experimental data at full-scale chord-based Reynolds numbers, $Re_C = U_0 C/\nu$ (where U_0 is the flow speed far upstream of the foil, C is the foil chord, and ν is the kinematic viscosity of the flowing liquid). Few experimental results exceed Re_C of several million while many applications lie in the Re_C range of 30 million to 100 million.

This paper presents the results of an experimental study of the flow over a two-dimensional hydrofoil for Re_C values from near 1×10^6 to more than 50×10^6. The foil has a nearly flat pressure side and a NACA-16 suction side modified with a rounded trailing edge bevel of apex angle 44° (geometry I) or 56° (geometry II). The foil section is typical of naval propeller blades of moderate thickness and chamber, and was chosen for its application-relevance and its potential for *Re*-dependent flow features. In particular, three-dimensional propeller design techniques often rely on two-dimensional section performance data (Kerwin 1986). Also, the trailing-edge bevel – typically introduced on propeller blades for structural integrity during severe off-design operations – leads to a compact region of flow separation whose characteristics depend on bevel geometry and Reynolds number. The present experimental effort is concentrated on this near-trailing-edge region, and the results reported here augment the available measurements of flat-plate boundary-layer flows (DeGraaff & Eaton 2000; Österlund *et al.* 2000) suitable to test high-Reynolds-number exterior-flow models.

The principal goals of this study were to identify phenomena that affect foil performance at high Reynolds number, and to provide a comprehensive data set for validation of high-Reynolds-number numerical models. Here, foil performance includes lift, drag and the prevalence of near-wake vortex shedding, an important hydroacoustic noise source for non-cavitating lifting surfaces (see Blake 1986; Blake & Gershfeld 1989; or Howe 1998). The measurements reported here document only the time-averaged flow over the foil, but even these results display interesting Reynolds-number dependences resulting from the interplay of boundary-layer transition, flow separation and wake formation. Featured prominently in this interplay is the phenomenon of near-wake vortex shedding, though these findings are beyond the scope of this paper.

Prior results documenting the mean flow at low Mach number on foils, struts and turbine blades has been largely motivated by the need to understand and predict lifting-surface performance, and possibly eliminate vortex shedding. Early work in this area, particularly for compact bodies, is reviewed in Bearman (1965); a more recent review is provided in Blake (1986). Mean velocity profiles in the boundary layer and in the near wake of minimally lifting struts are provided in Blake (1975) for Re_C of $\sim 2 \times 10^6$. The findings of the present effort are similar to these but extend the range of experimental Re_C to more than 50×10^6 and include the influence of lift. More recent work on individual foils and struts experiencing steady inflow conditions has been computational (Wang & Moin 2000, 2002), but again, at lower Re_C than reached in the present studies. This situation is similar for unsteady foil-flow studies (Ho & Lakshminarayana 1997; Luire, Keenan & Kerwin 1998) where Re_C only as high as 4×10^6 has been investigated.

Low-Mach-number airfoil studies cover many of the same phenomena as presented in this paper. Boundary-layer transition on airfoils is reviewed in Malick (1997) and a recent prediction technique is presented in Brodeur & van Dam (2000). Experimental studies of steady (Bastedo & Mueller 1986; Fitzgerald & Mueller 1990) and unsteady (Covert & Lorber 1982) boundary-layer separation have been conducted at Re_C values from 0.14×10^6 to 0.7×10^6. Mean and turbulent flow fields in the vicinity of boundary-layer separation on an asymmetric trailing edge in a two-stream wind tunnel are reported in Thompson & Whitelaw (1985). Here, at $Re_C \sim 2 \times 10^6$, it was determined that the boundary-layer flow that enters the separated region near the trailing edge significantly influences the development of the wake. The present study shows that this result persists at higher Re_C. A general review of turbulent boundary-layer separation is provided in Simpson (1989).

Work on the performance of compressor and turbine blades and cascades has many similarities to the current study as well, including the emphasis on lift, drag, boundary-layer development, trailing-edge characteristics and near-wake vortex shedding. A review of this literature prior to 1987 is provided in a series of papers (Deutsch & Zierke 1987, 1988*a*, *b*) where experimental results at $Re_C = 0.5 \times 10^6$ are reported. More recent experimental (Umbaldi *et al.* 1996; Halstead *et al.* 1997*a*) and computational (Halstead *et al.* 1997*b*) efforts cover single- and multi-stage cascades at Re_C up to 1.6×10^6 and 0.6×10^6, respectively. In addition, measurements of boundary-layer transition and separation conducted on flat plates at turbine-blade conditions are reported in Volino & Hultgren (2000) for plate-length-based Reynolds numbers up to 0.3×10^6.

All of the experimental work described above on foils, struts and blades involves test models having Re_C values at or below 4×10^6. Furthermore, prior steady-flow results at or above $Re_C = 2 \times 10^6$ involve minimally lifting struts with section lift coefficients that fall below that typically sought for propeller blades or aircraft wings. By comparison, the current test model generated significant lift forces, and represents an important step towards the understanding of practical three-dimensional propeller blades. Moreover, the Re_C values in the current experiments are high enough to comfortably span the gap between the prior studies and many full-scale applications.

The remainder of this paper presents our results, observations and analysis of the time-averaged low-Mach number flow over a two-dimensional hydrofoil with two different trailing edges. Section 2 describes the test model, flow facility, experimental apparatus and measurement techniques. Section 3 provides the results for the mean flow upstream, on the surfaces, and in the wake of the hydrofoil, with emphasis on the trailing-edge region under variations of Reynolds number and geometry. These

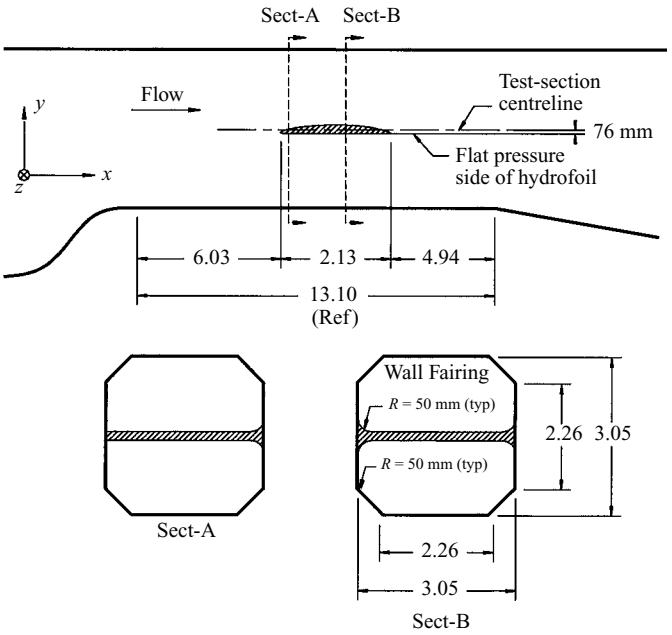

FIGURE 1. The test-section geometry and hydrofoil mounting location, shown in an elevation view looking spanwise and two section views looking downstream. All dimensions are in metres unless otherwise noted, and the test-section dimensions are referenced to the inside surface. Optical access at the leading and trailing edges required omission of the wall fairing fillet radii on the wall at $z/S = 0$ in the ranges $x/C < 0.19$ and $x/C > 0.87$. This configuration is depicted in Section-A. The ends of the remaining length of wall fairing were smoothly tapered.

data are used to determine how the growth of boundary layers on the suction and pressure sides of the hydrofoil influence the separated region at the trailing edge. Section 4 discusses these results and attempts to link the observed phenomena to well-established Reynolds-number trends in turbulent wall-bounded flows and wakes. The final section summarizes the effort and presents the conclusions drawn from this work.

2. Experimental set-up and techniques

The high Reynolds numbers of this experiment were achieved with a large hydrofoil tested in the US Navy's William B. Morgan Large Cavitation Channel (LCC). The LCC is a low-turbulence recirculating water tunnel with a $3.05\,\mathrm{m} \times 3.05\,\mathrm{m} \times 13\,\mathrm{m}$ test section and is capable of steady flows from 0.25 to $18.3\,\mathrm{m\,s^{-1}}$ (Etter & Wilson 1992). The hydrofoil spanned the test section and was mounted near its geometric centre (see figure 1). Gaskets at the hydrofoil–wall junction prevented bypass flow, and tunnel blockage based on the hydrofoil's maximum thickness (0.171 m) was 6%. The ratio of the foil chord to the vertical test-section dimension was 0.70. The foil's angle of attack, α, was measured between the tunnel axis and the flat pressure side of the hydrofoil. For all results reported here, the foil was mounted at $\alpha = 0^\circ$, measured within an estimated uncertainty of $\pm 0.05^\circ$. At the maximum flow speed of $18.3\,\mathrm{m\,s^{-1}}$ and $\alpha = 0^\circ$, the hydrofoil generates approximately 590 kN (60 metric tons) of lift. At this speed and the facility's limit on water temperature (104 °F), a maximum Re_C value of 61×10^6 was achieved.

Testing was conducted in three experimental campaigns (separate testing periods of approximately six-week duration) with the first campaign measurements limited to laser-Doppler velocimetry (LDV). Between the first and second testing campaigns, debris was discovered in the LCC's flow management section, and an assessment has been made of its impact on the test results. Measurements from the first campaign (with debris) showed spatial variation in the time-averaged inflow free-stream velocity of approximately $\pm 1\%$, over the measured flow range of 3 to 18.3 m s^{-1}. Measurements of the root-mean-square (r.m.s.) of free-stream velocity near the leading edge of the hydrofoil, though insufficient to fully characterize the inflow turbulence, limit its value to $\pm 1.5\%$ of the velocity far upstream. After debris removal, extensive free-stream uniformity and turbulence measurements were made in the empty test section at a streamwise location corresponding roughly to the hydrofoil's leading edge. Over the full range of facility flow speeds, spatial variation of the mean free-stream velocity was within $\pm 0.5\%$, and the r.m.s. of free-stream velocity was within 0.5% of the velocity far upstream (J. M. Cutbirth & J. T. Park, personal communication 2002). These conditions apply to the second and third testing campaigns in which selected trailing-edge LDV measurements were repeated and all other data were acquired. Though the debris measurably affected inflow uniformity and may have elevated free-stream turbulence, a critical comparison of the LDV measurements repeated between campaigns did not reveal flow variation exceeding experimental uncertainty.

The hydrofoil test model was cast from nickel-aluminium bronze, machined to the specified shape (S. Jessup, personal communication 1999) and polished to a r.m.s. surface roughness of 0.25 μm. Using flat-plate boundary-layer scaling, this roughness represents $k^+ < 1$ at the highest test speed, and thus the clean foil may be considered hydrodynamically smooth (White 1991). However, for particle imaging velocimetry (PIV) flow measurements the tunnel was flood-seeded with silver-coated glass spheres of 16 μm mean diameter. The gradual accumulation of these particles varied the effective surface finish of the hydrofoil, and the large tunnel drain and fill times made frequent cleaning impractical. The diameter of these particles was equivalent to $k^+ \sim 20$ at the highest Re_C tested. As will be discussed in § 3.2, these particles may have affected boundary-layer transtition. Otherwise, no boundary-layer tripping device was employed.

The hydrofoil cross-section is depicted in figure 2, and numerical coordinates of the surface points defining the shape of the airfoil used in this study are provided in table form in an Appendix†. Both the figure and coordinates reflect a hypothetical sharp trailing edge. In reality, a 0.4 mm radius was applied to the geometry specified, reducing the chord by a negligible amount. Figure 2(*a*) also defines the coordinate frames used in this paper. In the tunnel coordinate frame, the streamwise coordinate, x, is defined by the tunnel axis, and vertical coordinate, y, is taken normal to x. (The spanwise coordinate, z, completes the set of right-handed Cartesian coordinates.) The vertex of the trailing-edge bevel angle is defined as the coordinate $(x/C, y/C) = (1, 0)$. In the surface-aligned coordinate frame, the t-coordinate is defined by the local surface tangent with the h-coordinate taken normal to t. Finally, some results are presented in a rotated Cartesian coordinate frame defined by h and t at 93% chord. This frame is designated the trailing-edge coordinate frame.

† Available as a supplement to the online version or from the authors or the JFM Editorial office, Cambridge.

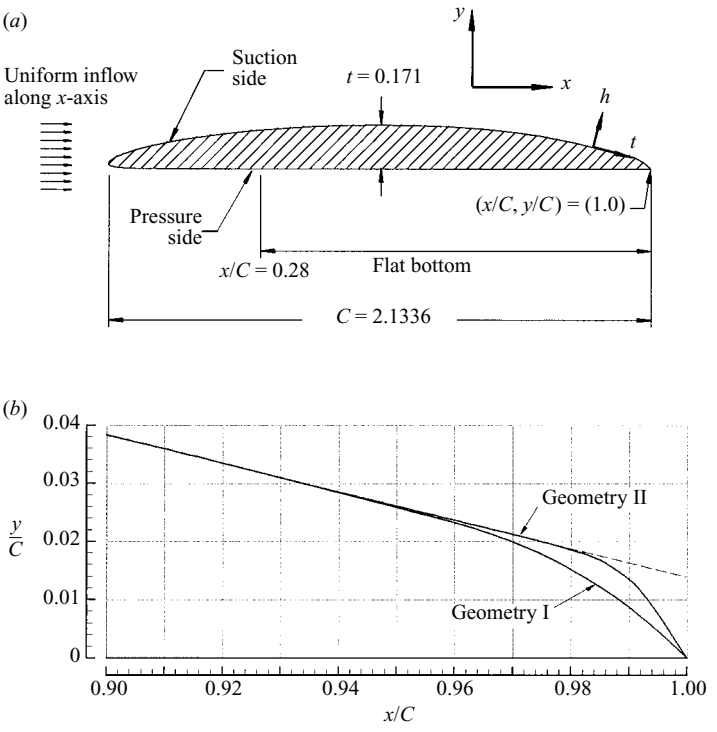

FIGURE 2. (*a*) The cross-section of the geometry I hydrofoil with chord and maximum thickness indicated. The chord length given is the idealized value, measured to the vertex of the trailing-edge apex angle. This point defines $(x/C,\ y/C) = (1, 0)$ in the tunnel coordinate system, for which the x-axis is taken as the streamwise axis of the tunnel. Also depicted is the hydrofoil coordinate system, for which the t-axis is taken as the local surface tangent. (*b*) A detail of the geometries I and II trailing edges. The 0.4 mm radius, applied to the trailing-edge tip, is not depicted. The dashed line indicates the direction of the surface tangent at $x/C = 0.930$.

A bolt-on trailing-edge modification was used to vary the suction side bevel geometry. The two bevel designs tested are shown on figure 2(*b*); the more streamline trailing edge, geometry I (bevel radius, $R_B = 76.2$ mm and apex angle, $\beta = 44°$), and the more bluff trailing edge, geometry II ($R_B = 38.1$ mm, $\beta = 56°$). Both geometries generate suction side boundary-layer flow separation in the last 2% of the chord. Laser-based metrology on the finished geometry-I hydrofoil confirmed a typical tolerance of ± 0.2 mm and a maximum tolerance of ± 0.5 mm between the as-designed and as-built geometries. The trailing edge of geometry II, which was applied in the field, could not be constructed to such a high tolerance. Therefore, the geometry given in figure 2(*b*) and Appendix A is the as-built geometry, measured to within ± 0.5 mm.

The hydrofoil experiments were conducted using well-established water-tunnel testing techniques for fluid velocity and static pressure measurements. Test-section pressure was held constant and sufficiently high to suppress significant cavitation. Test-section flow speed was controlled through the rotational velocity of the tunnel's axial-flow impeller and monitored by a fixed LDV probe. Tunnel water temperature was monitored, but not controlled; it increased by as much as $1.3\,°\mathrm{C\,h^{-1}}$ during tests at $18.3\,\mathrm{m\,s^{-1}}$ and varied between 24 °C and 40 °C over the course of the tests. As a result, water viscosity and the Re_C achieved at a given test speed varied by as much as 20%.

U_0 (m s^{-1})	Re_C (million)	Symbol/line-type
0.5	1.4	– – –■– – –
1.5	4	—▲—
3.0	8	– - – -▼- – - –
6.0	17	- - -▶- - -
12.0	33	···◀···
18.3	50	·· –··●·· – ··

TABLE 1. Upstream flow velocities and nominal Re_C with symbol and line-types listed. In the figures of this paper, filled and open symbols correspond to trailing edge geometries I and II, respectively.

Table 1 gives the nominal Re_C values based on an average water temperature of 32 °C. Measurements of vibration in a bandwidth from 2 Hz to 1 kHz were made with eight accelerometers (Wilcoxon 754-1) distributed within the hydrofoil. These measurements confirmed that the hydrofoil was effectively rigid, even when unsteadiness developed in the foil's near wake.

Static pressure measurements were made on the hydrofoil using 30 taps distributed along the suction and pressure side surfaces. Each tap was progressively offset in the spanwise direction by 40 mm, and all taps were contained within the middle 50% of the span. Leading-edge taps at $x/C \leqslant 0.03$ were 0.8 mm in diameter and the remaining taps were 1.6 mm in diameter. The measurements were made with a Rosemont differential pressure transducer (3051CD, $\pm$250 kPa, differential) referenced to a 1.6 mm diameter tunnel wall tap at $x/C = -2.38$, and routed to individual hydrofoil taps with a rotary sampling valve (Scanivalve J-type). The pressure transducer was calibrated with a pressure standard (Paroscientific 740 DigiQuartz, 124 kPa, differential) of accuracy $\pm$12 Pa. Significant sources of static pressure measurement uncertainty include (i) uncertainty in the calibration method, (ii) transducer nonlinearity, (iii) zero bias, and (iv) hole error (see Benedict 1984). At $Re_C = 50 \times 10^6$, hole error governs, and the overall uncertainty is $\pm$0.006 in pressure coefficient units. At $Re_C = 4 \times 10^6$, and excluding zero bias, calibration error governs, and the overall uncertainty is $\pm$0.015. However, at all but the highest Re_C, transducer drift between calibrations produced zero bias in excess of the other uncertainties. The LCC's flow deceleration time precluded zero-flow measurements at a frequency sufficient to address this zero bias. Consequently, corrections for zero bias have been made by matching the pressure coefficient near mid-chord (average of the three mid-chord taps) on the hydrofoil's pressure side to that on the geometry I hydrofoil at $Re_C = 50 \times 10^6$. This method produces static pressure distributions that are consistent with the steady Bernoulli equation using LDV-acquired velocities outside the boundary layer on the pressure side of the trailing edge and on the suction side near mid-chord. The method also yields pressure coefficient values at the leading-edge tap consistent with the free-stream stagnation pressure. Computation of pressure gradients, lift and drag are not affected by the zero-bias error correction.

Static pressure measurements were also made on the walls and ceiling of the test section. Wall taps extended along three lines from $-3.0 < x/C < 3.0$ at $y/C = -0.19$, 0.04 and 0.26, respectively. Single taps were located at mid-span on the test section ceiling ($y/C = 0.71$) at $x/C = 0.0$, 0.5 and 1.0. All wall and ceiling taps were 1.6 mm in diameter and were routed via solenoid-actuated ball valves to a second differential

Measurement station	Extent of measurements		
	Streamwise, x/C	Vertical, v/C	Spanwise, z/S
1 Inflow plane	-2.3	$-0.20 < y/C < 0.28$	$0 < z/S < 0.5$
2 Leading edge	-0.014	$-0.20 < y/C < 0.28$	0.25
3 Suction side boundary layer near mid-chord	Origin at $x/C = 0.43$	$0 < h/C < 0.01$	0.35
4 Boundary layer approaching trailing edge	0.93	$-0.20 < y/C < 0.28$	0.25
5 PIV field at trailing edge	$0.96 < x/C < 1.11$	$-0.025 < y/C < 0.030$	0.36
6 Near-wake plane	1.028	$-0.20 < y/C < 0.28$	$0 < z/S < 0.5$
7 Far wake	1.42	$-0.20 < y/C < 0.28$	0.25

Table 2. PIV and LDV velocity survey locations.

pressure transducer (Rosemount 3051P, 6350 mm water differential). For the tunnel wall pressure data, zero-flow measurements were used to correct the transducer zero bias. At $Re_C = 50 \times 10^6$, the overall uncertainty is governed by hole error and is estimated to be ± 0.006 in pressure coefficient units. At $Re_C = 4 \times 10^6$, the uncertainty of the calibration governs and the overall uncertainty rises to ± 0.015.

Flow velocities above and below the foil were measured with three systems: (i) a two-component Dantec LDV at 0.25 span, (ii) a two-component PIV system at 0.36 span and (iii) a miniaturized one-component LDV probe (Fourguette *et al.* 2001) housed within the hydrofoil body at $x/C = 0.43$ and 0.35 span. Table 2 provides the LDV and PIV measurement locations. Results from all three systems were normalized by the flow speed upstream of the foil, U_0, measured at $x/C = -2.38$ with a dedicated one-component Dantec LDV system. To support LDV acquisition in all three testing campaigns, the LCC was flood-seeded with silicon carbide particles of 2 μm mean diameter. To support PIV acquisition in the second and third testing campaign, the channel was additionally seeded in much higher density (0.004 kg m^{-3}) with silver-coated glass spheres of 16 μm mean diameter (Potters Industries, SH400S33).

The fixed and traverse-mounted LDV systems used Dantec components including signal processors (BSA57N11), fibre optic probes, a three-dimensional probe traverse and control software. Laser light was provided by two 6 W argon-ion lasers (Spectra Physics 2016 and 2017). The external two-component LDV used a Dantec optical head having 111 mm beam spacing and a 1600 mm (in air) focal length. The head was mounted on a large traverse and provided an in-water focal volume of approximately 170 μm in diameter and 6 mm in length. The traverse and the test-section windows allowed LDV data collection over approximately the middle 1 m of the test-section height. This LDV system was calibrated as a unit using a rotating disk to generate the velocity standard and separate calibrations were used for low speeds ($Re_C = 17 \times 10^6$ and below) and high speeds ($Re_C = 33 \times 10^6$ and 50×10^6). The uncertainty in locating the disk centre is the dominant source of velocity bias error, and generates uncertainties of ± 0.04 m s^{-1} and ± 0.08 m s^{-1} (at the 95% confidence level) for the low- and high-speed calibrations, respectively. In comparison with bias error, random error is negligible. To estimate the uncertainty in the normalized velocity data, a distinction must be made between results for which data are taken and normalized by a single LDV system, and data taken and normalized using separate systems. In the former, the uncertainty in the normalized value is 0.08 and 0.004 in normalized units

at $Re_C = 1.4 \times 10^6$ and 50×10^6, respectively. In the latter, uncertainties are generally higher.

To select the best spanwise location for the LDV measurements, the spanwise uniformity of the geometry 1 hydrofoil flow was assessed. Measurements at $Re_C = 8 \times 10^6$ and 50×10^6 were collected on a coarse grid (50 mm × 50 mm) in a plane perpendicular to the flow direction at fixed x-locations far upstream of the foil and just aft of the trailing edge (Bourgoyne *et al.* 2001*a*). Within the resolution of the grid, these measurements showed the time-averaged flow to be two-dimensional over the middle 90% of the foil span. (Side-wall contamination extends out to only 5% span on each side.) Motivated by the higher LDV data rates near the test section windows, this finding was used to justify collection of the remaining LDV at $z/S = 0.25$. (Further findings concerning spanwise uniformity are presented in § 3.4.)

Measurements in the trailing-edge region were taken to confirm repeatability between campaigns. These revealed that the first campaign LDV measurements differed from those of the second two campaigns by a consistent factor of 1.04. This difference was traced to the calibration of the upstream LDV system that monitored U_0. (Owing to this error, the normalized velocity data published in Bourgoyne (2001*a*) is overstated by a constant factor of 1.04.) The error was systematically corrected using comparisons between the measurements of U_0 from the fixed single-component LDV and the measurements of the local free-stream velocities from the traverse-mounted two-component LDV. The correction method relies on the assumption of negligible Re_C-dependence in the local free stream at coordinates $y/C > 0.26$. Following this correction to U_0, all LDV velocity statistics from all three campaigns match within experimental uncertainty.

Planar PIV instantaneous flow-field measurements in the vicinity of the hydrofoil trailing edge were made using a LaVision Flowmaster-3S PIV/PTV system, including two digital cameras (1280 × 1024 pixels) and a PC-based data acquisition system. Light was provided by two flash-lamp-pumped Nd-YAG lasers (Spectra Physics Pro 250-10) delivering 800 mJ per pulse at 532 nm. The laser sheet was masked to 3 mm thickness and relayed downward through the top of the LCC test section to illuminate the suction-side trailing edge and near wake. The pressure side of the hydrofoil was not illuminated. Owing to test section geometry, the laser sheet could not be installed at the spanwise location of the LDV and was instead installed at the nearest practical location ($z/S = 0.36$). The two cameras were operated in tandem at a magnification of 0.1 mm/pixel to capture a composite field of view. Camera depth of field exceeded the light-sheet thickness. Raw images from the two cameras were processed individually using LaVision's DaVis v6.0.4 analysis software in cross-correlated mode with 32 × 32 pixel interrogation areas. Accordingly, each PIV vector produced is the result of particle-pair averaging over a cube of flow of side ≈3 mm. Images were acquired at a rate of approximately 1 Hz.

The PIV image magnification was optimized to capture in a single frame the wake physics of interest and produce typical particle image diameters of 3 pixels. The optimal time between images was governed by the low velocities in the recirculating region of the near wake, and produced a field-averaged particle displacement of approximately 7 pixels. This determined the minimum suitable interrogation area of 32 × 32 pixels, typically capturing 10 particle pairs. The raw images were good. For example, when processed with a single-pass calculation for each interrogation area, they produced vector fields with less than 10% erroneous vectors and an average peak ratio (ratio of the magnitudes of highest and second-highest cross-correlation peaks) of 1.8. When processed with an adaptive multi-pass algorithm, the percentage

of erroneous vectors dropped to less than 3% and the average peak ratio improved to 2.6. In the plots presented in this work, the adaptive multi-pass algorithm was used and vectors with high uncertainty ($Q < 1.8$) were dropped from the sample population.

PIV uncertainties include random and bias error in the velocity measurements and bias error in the spatial location of these velocities. Assuming a characteristic subpixel resolution of ± 0.25 pixels, the uncertainty due to random error in the velocity magnitude derived from particle pairs with a 7-pixel displacement is $\pm 3\%$. This estimate is supported by the measured self-consistency of the PIV. Specifically, images of a particle field were taken simultaneously with different cameras and processed by the same PIV algorithm. Comparison of the resulting instantaneous vector fields produced an L_2 error norm of 3% for the velocity magnitudes. An identical comparison of the time-average of 500 instantaneous fields yielded an L_2 error norm of less than 1%. The reduction in the error norm by time-averaging confirms the predominately random nature of the error and supports the estimate of $\pm 3\%$ random error.

Bias error in the PIV velocities is introduced through uncertainty in image scaling. Images of a precision calibration grid mounted to the submerged hydrofoil (in the absence of flow) provided this scale with approximately $\pm 1\%$ accuracy. Velocity uncertainty is also introduced through the normalization velocity, U_0 acquired with the upstream reference LDV, discussed earlier. The combined effect of these sources of error is a characteristic uncertainty of the normalized mean PIV velocities of $\pm 1.5\%$. Note that this estimate is overstated in regions of high velocity and understated in regions of low velocity.

Simultaneous images from the two cameras are located relative to one another within ± 0.2 pixels using a PIV correlation of the overlapping region of the images. The composite velocity field is then located relative to the foil within ± 2 pixels (± 0.2 mm) using the image of the trailing-edge surface and its laser sheet shadow.

3. Results

Experimental data were collected for both trailing-edge geometries for zero angle of attack at the flow speeds and nominal Reynolds numbers given in table 1. This table also includes the symbols and line types used in the remainder of this paper to designate Re_C values. Geometry I and II results are reported with filled and open symbols, respectively. The presentation of results follows in subsections devoted to: static and dynamic foil deflections; static pressure profiles; outer (potential) flow results; and inner (viscous) flow results.

3.1. *Hydrofoil deflection and vibration*

Though the foil was made of solid metal and mounted with the greatest practical rigidity, the static lift at $Re_C = 50 \times 10^6$ and $\alpha = 0$ deflected the trailing edge 8 mm at the midspan. At $Re_C = 33 \times 10^6$, this deflection decreased to 3.5 mm. Leading-edge static deflections were not measured, but should approximate those of the trailing edge based on the near-symmetry of the hydrofoil's cross-section, lift distribution and mounting scheme. Also based on the mounting scheme and system symmetries, the spanwise dependence of the static deflection should approximate that of a simply supported beam under a uniform load. Deflection of this kind may potentially affect the hydrofoil flow. However, the ratio of the maximum mid-span deflection to the

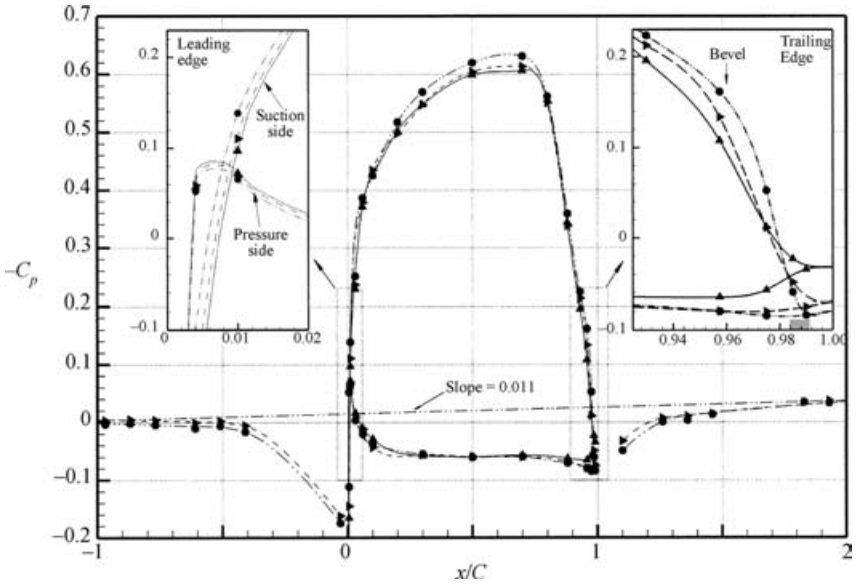

FIGURE 3. The static pressure coefficient, C_p, on the hydrofoil surface and on the vertical centreline of the test-section sidewalls ($y/C = 0.04$) for geometry I at Re_C of 4×10^6, 17×10^6, and 50×10^6. The stagnation pressure ($C_p = 1.0$) was measured at $x/C = 0$ but is not shown. The insets present at larger scale the data near the leading and trailing edges. Within the trailing-edge inset, the x/C at which the suction side bevel initiates is labelled, and the region of mean suction-side flow separation is indicated by a grey bar on the x/C axis. Symbols represent the measured static pressure. Lines represent a cubic spline of the measured values. The straight line near zero C_p connects the wall data at the beginning and end of the hydrofoil influence.

total hydrofoil span is less than 0.002. For such small deflections, the flow field is presumed to locally approximate that of the undeflected shape.

Measured fluctuating acceleration levels increased rapidly with flow speed, but were broadband and did not suggest problems with flow-excited oscillations of foil-tunnel structural modes. At $18.3\,\mathrm{m\,s^{-1}}$ (the worst case), the highest r.m.s. surface-normal vibratory speed recorded by any of the eight accelerometers was $1.5\,\mathrm{mm\,s^{-1}}$. This r.m.s. velocity is less than 0.01% of U_0, significantly below the turbulence level of the water tunnel. In addition, the greatest observed change in vibration level occurred between flow speeds of 12 and $18.3\,\mathrm{m\,s^{-1}}$ yet the differences between the normalized mean flow fields at these speeds are well within experimental uncertainty. Together these observations suggest that foil vibration was insignificant in these experiments.

3.2. *Static pressures*

The pressure coefficient, $C_p = 2(P - P_0)/\rho U_0^2$ where P is the measured static pressure and ρ is the water density, was measured on the surface of the hydrofoil and on the walls of the LCC test section. The reference pressure P_0 was measured at the same upstream location as the reference velocity U_0. Measured C_p values for Re_C between 4×10^6 and 50×10^6 are shown in figures 3 and 4 for geometries I and II, respectively. Following convention, the vertical axes on these figures display $-C_p$; this places the suction side data in the upper half of each figure. For clarity, data at $Re_C = 8 \times 10^6$ and 33×10^6 are omitted from figure 3, and data from $Re_C = 17 \times 10^6$ and 33×10^6 are omitted from figure 4. In both cases, the omitted data fall monotonically between

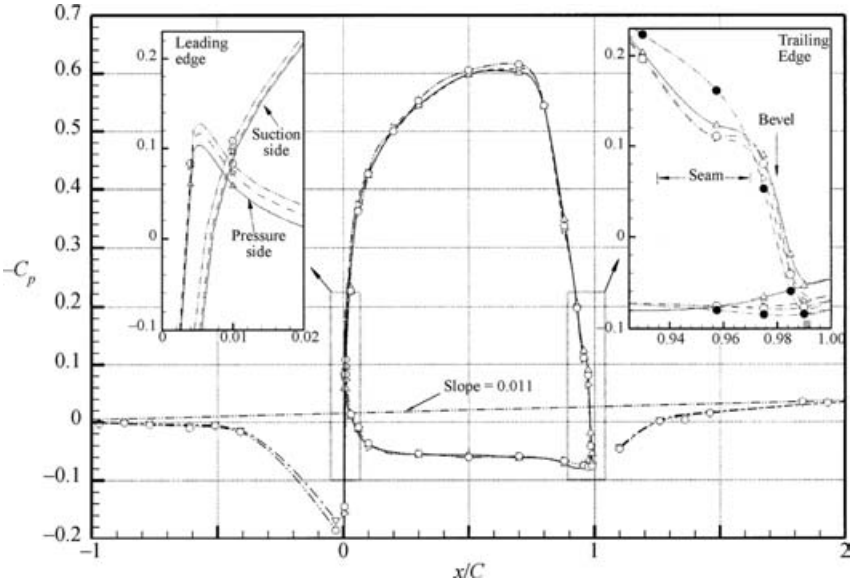

FIGURE 4. Static pressure coefficient, C_p, for the hydrofoil with the geometry II trailing edge, in a format similar to that of figure 3. Data at $Re_C = 17 \times 10^6$ are not available on the test-section walls and are replaced with data at $Re_C = 8 \times 10^6$ in the trailing-edge inset panel, the data from geometry I at $Re_C = 50 \times 10^6$ is also shown for comparison. Also indicated in the trailing-edge inset panel is the streamwise extent of the smooth seam between the hydrofoil and trailing-edge modification. The static pressure tap in this region does not have a square edge and therefore has higher uncertainty.

the plotted points for neighbouring Re_C values. The fitted curves are cubic splines constrained to pass within the uncertainty range of each data point. For each flow speed, the C_p value at $x/C = 1$ was extrapolated from the suction and pressure side measurements nearest the trailing edge. Variations in the static pressure distributions between measurements at different values of Re_C are small, and are most discernable near the foil's midchord and trailing edge. The left-hand and right-hand inset panels in figures 3 and 4 show the leading- and trailing-edge C_p-data at greater scale, with the location of the suction side separation shown as a shaded region on the x/C axis. The sharp changes in C_p-curve slope near the trailing edge are nearly coincident with the initiation of the suction side bevel depicted in figure 2(*b*) and denoted by 'Bevel' on the right-hand side insets of figures 3 and 4. Note that the suction side tap at $x/C = 0.958$ with the geometry II fell within the faired seam of the trailing-edge modification and did not have a sharp-edged hole. As a result, the measurements there have increased uncertainty.

A comparison of figures 3 and 4 shows that the C_p measurements are similar, but there is less variation with increasing Re_C with geometry II. As might be expected from the geometrical difference, geometry II allows the foil to maintain a negative suction-side C_p to greater x/C, but then the C_p turns positive with a steeper pressure gradient as x/C approaches unity. On both trailing edges, the pressure gradient just prior to boundary-layer separation becomes less adverse with decreasing Re_C, a trend linked to the decrease in the $-C_p$-peak near midchord on the suction side. For both edges, the C_p at $x/C = 1$ (the base pressure coefficient) decreases with decreasing Re_C, an indication that the near-wake dynamics are changing over this Re_C range.

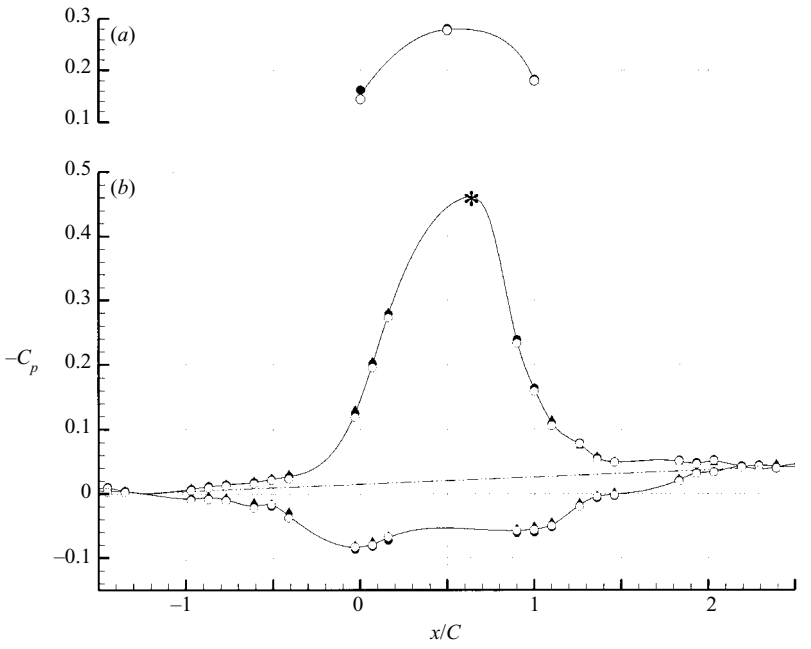

FIGURE 5. Static pressure coefficient, C_p, on the test-section walls and ceiling, for both trailing edges at Re_C of 4×10^6 and 50×10^6, in a format similar to figure 3. (*a*) Data from the test-section ceiling, and (*b*) data from the sidewalls on the suction side ($y/C = +0.26$) and pressure side ($y/C = -0.19$) of the foil. Symbols plot measured values and the solid line splines the average of the plotted points. Hydrofoil mounting hardware prevented data collection on the sidewalls near midchord, and the suction side point at $x/C = 0.65$ (denoted by $*$) is the average of the measured value on the suction side foil surface and the test-section ceiling at $Re_C = 50 \times 10^6$. The straight line near zero C_p is taken from figure 3, and connects the centreline wall data ($y/C = 0.04$) at the beginning and end of the hydrofoil influence.

Specifically, the dynamic flow measurements reveal a correlation between reduced base pressure and increased proximity to the trailing edge of developed pressure side vortices (not shown here). A similar relationship was demonstrated by Bearman (1965) for blunt bodies with splitter plates, and is consistent with the increase in drag generally associated with vortex shedding. The *Re*-dependence of the base pressure is weaker for geometry II.

Figure 5 presents C_p measured on the tunnel walls above ($y/C = 0.26$) and below ($y/C = -0.19$) the foil for $Re_C = 4 \times 10^6$ and 50×10^6 for geometry I, and at $Re_C = 50 \times 10^6$ for geometry II. The foil's mounting system prevented the collection of wall pressure data near mid-chord, so an interpolated data point ($*$) has been added at the x/C of foil's peak C_p. This value is the average of the measurements on the foil surface and water-tunnel ceiling at the given x/C. With this point, the splined C_p-curves and measured velocities conserve vertical momentum in a control volume enclosing the foil and described in § 4.5. Here, variation in C_p with Re_C and trailing-edge geometry is less than experimental uncertainty except very near the foil.

The foil's lift and test section blockage both contribute to static pressure variations on the test-section walls. Given the length of the foil's chord compared to the transverse test-section dimension, the lift on the foil produced by bound circulation was determined by the upstream flow speed and the confining effects of the test-section walls. At matching free-stream speeds, foil lift would be lower in an infinite

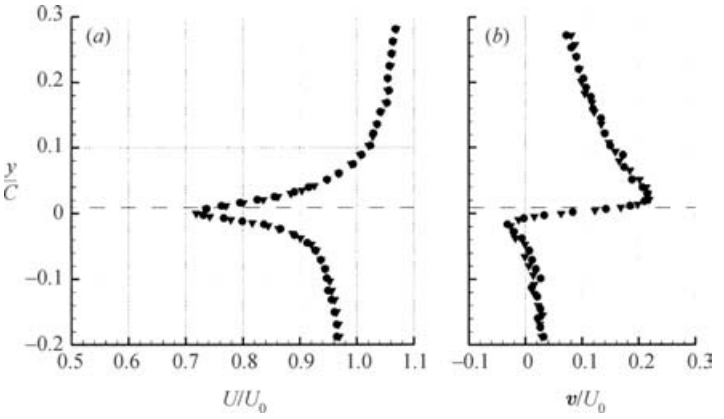

FIGURE 6. The flow near the leading edge ($x/C = -0.014$) of the geometry I hydrofoil, presented as the (a) streamwise and (b) vertical components of the time-averaged velocity, normalized by the velocity far upstream, U_0. The dashed line indicates the location of the vertical tangent of the leading edge ($y/C = 0.009$). Data is shown for $Re_C = 8 \times 10^6$ and 50×10^6. Data for $Re_C = 17 \times 10^6$ and 33×10^6 are omitted for graphical clarity, but collapse with the data shown.

environment. The measured C_p, on the ceiling of the test section directly above the foil (−0.28, see figure 5a) can be used to determine the foil's lift to within a few per cent using of a two-dimensional vortex to represent the foil's bound circulation, a source and sink to represent the foil's thickness, and the method of images to account for the tunnel walls.

3.3. *Outer mean flow*

The measurements presented in this section document the global flow around the geometry I foil, specifically the tunnel-confined potential-flow. Based on the minimal geometry-dependence of the static pressure coefficient, this data is expected also to approximate the flow over the geometry II foil. These measurements are presented as vertical profiles of horizontal mean velocity, U, and vertical mean velocity, V, normalized by U_0. Data are presented at stations upstream of the foil, at the trailing edge, and downstream of the foil. The vertical extent of the measurements (see table 2) is the maximum afforded by the test-section windows. All data are for $z/S = 0.25$.

The upstream LDV-acquired average profiles of U and V are provided in figures 6(a) and 6(b), respectively, for $Re_C = 8 \times 10^6$, and 50×10^6 just upstream of the hydrofoil leading edge at $x/C = -0.014$. The foil's leading edge lies at $(x/C, y/C) = (0, 0.0092)$ and is indicated by the dashed line in the figure. The (U, V)-profiles at $Re_C = 17 \times 10^6$ and 33×10^6 are identical within data scatter to the results at $Re_C = 8 \times 10^6$ and 50×10^6.

Normalized mean flow velocities (U, V) above and below the foil near its trailing edge, at $x/C = 0.930$, 0.958 and 1.000 are shown in figure 7 for $Re_C = 8 \times 10^6$, and 50×10^6. Here, a small difference is seen in the data from the two plotted Re_C values, especially for U on the suction side of the foil. Measurements from $Re_C = 17 \times 10^6$ and 33×10^6 have been omitted for clarity. If shown, these data would fall smoothly and monotonically between the plotted data in figure 7. Velocity profiles from these three x/C locations have been included because they show the strong suction-side outer flow deceleration (compare figures 7a and 7e) that occurs near to, but upstream of, the trailing-edge bevel.

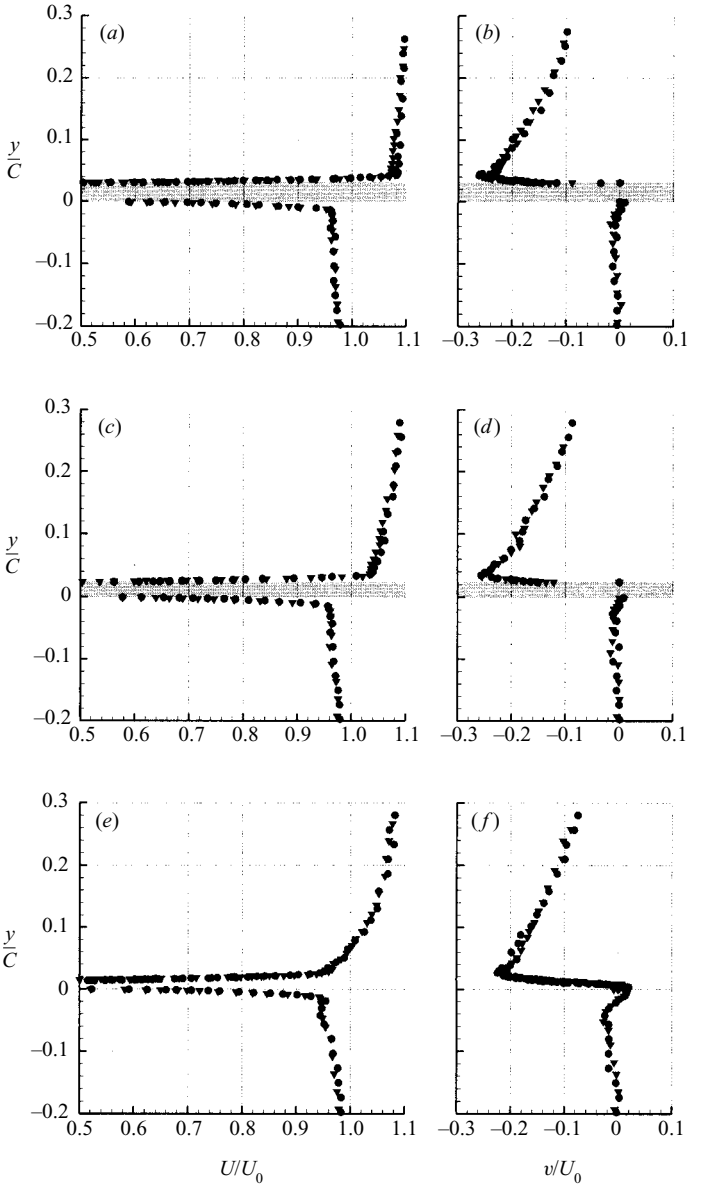

FIGURE 7. The boundary-layer flow on geometry I, presented in the same format as figure 6, and measured at (a,b) $x/C = 0.930$, (c,d) $x/C = 0.958$ and (e,f) $x/C = 1.000$. The location of the hydrofoil surface is indicated by the grey bar. A zero vertical velocity at the hydrofoil surface is assumed and plotted for clarity. Data are shown for $Re_C = 8 \times 10^6$ and 50×10^6. Data for $Re_C = 17 \times 10^6$ and 33×10^6 are omitted for graphical clarity, but trend monotonically in U_0 with the data shown.

Normalized mean flow wake profiles downstream of the foil at $x/C = 1.028$, 1.070 and 1.43, are shown in figure 8 for $Re_C = 8 \times 10^6$ and 50×10^6. As for the near-trailing-edge measurements in figure 6, only small differences are apparent between the data from these two values of Re_C, and the data from $Re_C = 17 \times 10^6$ and 33×10^6 (not plotted) fall smoothly and monotonically between the plotted results. At the farthest

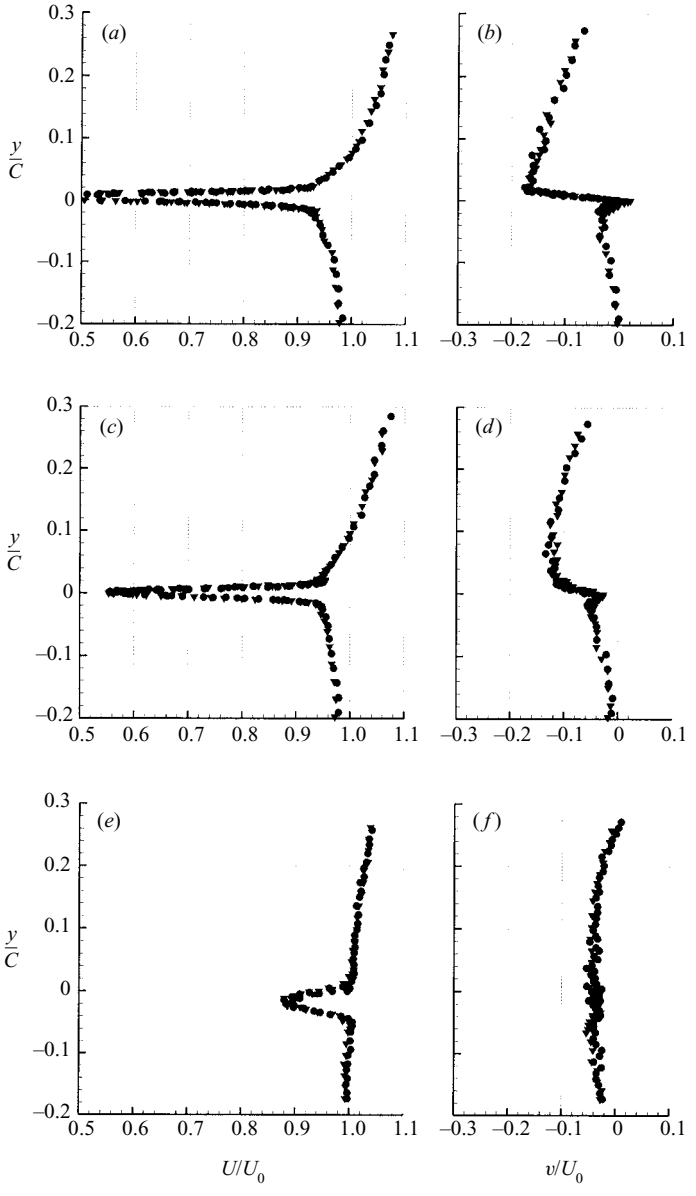

FIGURE 8. The wake flow of geometry I, presented in the same format as figure 6, and measured at (a,b) $x/C = 1.028$, (c,d) $x/C = 1.070$ and (e,f) $x/C = 1.430$. Data are shown for $Re_C = 8 \times 10^6$ and 50×10^6. Data for $Re_C = 17 \times 10^6$ and 33×10^6 are omitted for graphical clarity, but collapse with the data shown.

downstream location (figures 8*e* and 8*f*), evidence of the lift generated by the foil is apparent in the non-uniformity of U, and the negative average value of V. Here, the vertical extent of the measurements reported in figures 6 to 8 hides the details of the near-foil boundary layer and wake flows that have thicknesses of order $0.01C$. The next section presents measurements of the mean flow close to the foil surfaces.

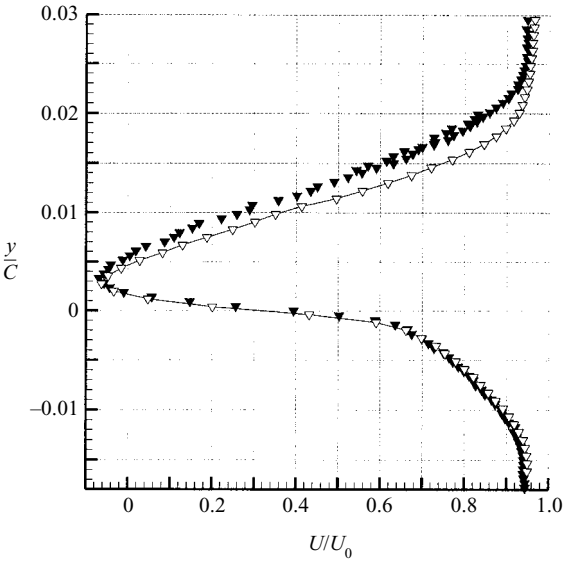

FIGURE 9. The near-wake flow of geometry I at $Re_C = 8 \times 10^6$, presented in the same format as figure 6, and measured at $x/C = 1.009$. Symbols are measured values: ▼, LDV at $z/S = 0.25$; —▽—, PIV at $z/S = 0.36$. Though pressure side measurements agree within experimental uncertainty, suction side measurements differ. The disagreement is attributed to spanwise variation in the location of suction side boundary-layer transition at this Re_C. The measurements are consistent with transition and separation occurring further upstream at $z/S = 0.25$ than at $z/S = 0.36$.

3.4. *Inner mean flow*

This subsection covers the measured boundary layer and near-wake mean flow close to the foil's trailing edge. In this flow region, the LDV results are complemented with PIV results, for which more flow conditions were measured. Unfortunately, a systematic comparison of the PIV and LDV data revealed inconsistencies.

The foil and its mounting system were intended to produce two-dimensional flow over as much of the foil's span as possible. However, unrepeatable variation in the mean flow was measured with the PIV system, particularly at $Re_C = 8 \times 10^6$. The observed behaviour is attributed primarily to uncontrolled variation with time and with spanwise location in the downstream location of suction side boundary-layer transition. Evidence to this effect is found in the reduction or disappearance of these measurement variations at the highest and lowest values of Re_C. At the highest values of Re_C, suction side transition is believed to occur uniformly close to the foil's leading edge. At the lower values of Re_C, suction side transition occurs uniformly near 70% chord where the adverse pressure gradient first becomes steep (see figure 25). Unfortunately, foil surface imperfections or the accumulation of PIV seed may have been controlling factors for suction side boundary-layer transition in the mid-range of Re_C of this study ($4 \times 10^6 \leqslant Re_C \leqslant 17 \times 10^6$). Though the effect is small in the attached boundary layers, the resulting variation in suction side boundary-layer separation appears to amplify the effect. Figure 9 shows the worst-case variations observed in the near-wake mean velocity profiles (geometry I at $Re_C = 8 \times 10^6$). The thicker wake profile in figure 9 is from the LDV measurements at 25% span. The thinner wake profile is from the PIV measurements at 36% span. The thinner PIV profile was never measured by the LDV system at this Re_C. In summary, some variation of the inner

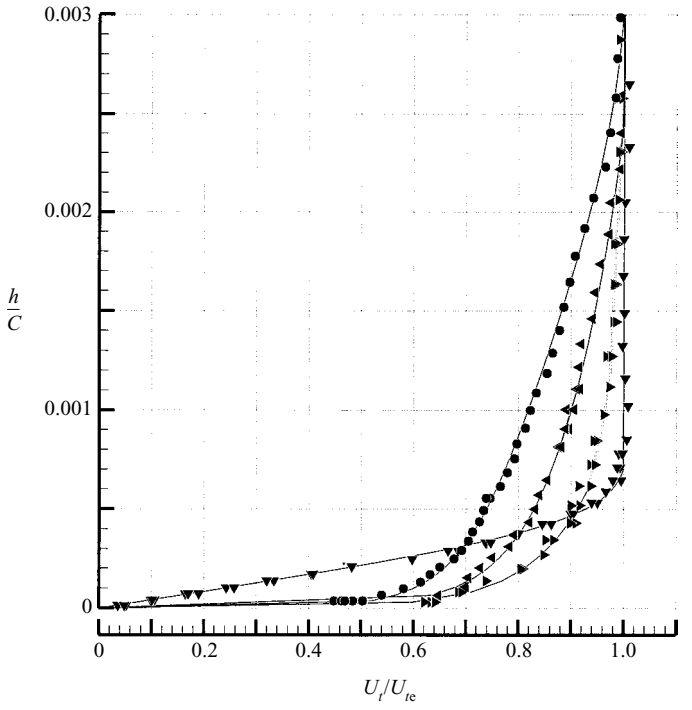

FIGURE 10. Component of the time-averaged velocity tangent to the surface at $x/C = 0.43$ on the suction side of the geometry I hydrofoil. Symbols are measured values and solid lines are fits through the data, using a laminar boundary-layer profile for $Re_C = 8 \times 10^6$, and a turbulent boundary-layer profile (equation 1) for $Re_C = 17 \times 10^6$, 33×10^6 and 50×10^6. At $Re_C = 17 \times 10^6$, the turbulent profile with Coles parameter, $\Pi = 0$, fits the data below $h/C = 0.006$. The data above $h/C = 0.006$ fit neither a laminar nor turbulent profile, but are traced with a solid grey line to improve graphical clarity. Table 3 provides the parameters used in the curve fits. All fits use $\kappa = 0.41$, $B = 5.5$ and $\nu = 0.775 \times 10^{-6}\ \mathrm{m^2\,s^{-1}}$.

mean-flow profiles at the trailing edge was observed at 36% span in the mid-range of Re_C of this study. To address this, the data presented have been restricted to the LDV mean flow measurements made at the 25% span location, and those PIV fields (measured at 36% span) that agree with these LDV measurements.

A measure of the viscous flow on the geometry I foil's suction side was provided by measurements of U_t (= the surface-tangent mean velocity) made at $x/C = 0.43$ with a miniaturized one-component LDV mounted inside the foil (Fourguette *et al.* 2001). These measurements are plotted in figure 10 for $Re_C = 8 \times 10^6$, 17×10^6, 33×10^6 and 50×10^6 along with laminar and turbulent boundary-layer profile fits. Following surface-aligned coordinates, h is the local surface normal coordinate and U_{te} is the surface-tangent mean velocity at the edge of the boundary layer ($h = \delta$) where δ is selected for a best fit for the boundary-layer profile. Here, δ and other fitting parameters, C_f = skin friction coefficient and Π = Coles' wake parameter, are given in table 3 for the Blasius profile fit at $Re_C = 8 \times 10^6$, and the Coles' profile fit (see White 1991),

$$U_t^+ = \frac{1}{\kappa} \ln h^+ + B + \frac{2\Pi}{\kappa} \frac{\sin^2(\pi h f/2\delta)}{\sin^2(\pi f/2)}, \tag{1}$$

Re_C ($\times 10^6$) nominal	U_0 (m s^{-1}) ± 0.01	δ/C ± 0.0001	U_{te}/U_0 ± 0.01	C_f ± 0.0002	Π ± 0.03
8	3.0	0.0007	1.25	0.0004	–
17	6.0	0.0022	1.26	0.0042	0.00
33	12.0	0.0025	1.27	0.0030	0.11
50	18.3	0.0030	1.27	0.0022	0.75

TABLE 3. Parameters of boundary layers near mid-chord ($x/C = 0.43$) on the suction side of the hydrofoil with trailing edge geometry I.

Re_C ($\times 10^6$) nominal	U_0 (m s^{-1}) ± 0.01	δ/C ± 0.0002	δ_e^{ss}/δ ± 0.01	U_{te}/U_0 ± 0.01	C_f ± 0.0002	Π ± 0.03	f
1.4	0.5	0.0103	1.13	1.12	0.0037	0.51	1.18
4	1.5	0.0072	1.28	1.12	0.0027	0.95	1.10
8	3.0	0.0103	1.18	1.10	0.0020	1.50	1.06
17	6.0	0.0113	1.11	1.10	0.0017	1.70	1.06
33	12.0	0.0113	1.11	1.10	0.0015	1.71	1.06
50	18.3	0.0113	1.08	1.10	0.0015	1.60	1.06

TABLE 4. Parameters of boundary layers approaching the trailing edge region ($x/C = 0.930$) on the suction side of the hydrofoil with trailing edge geometry I.

for the other values of Re_C. Here, the usual definitions apply: $U_t^+ = (U_t/U_e)\sqrt{2/C_f}$, $h^+ = hU_{te}\sqrt{C_f/2}/\nu$, $\kappa = 0.41$, $B = 5.5$, $\nu = 0.775 \times 10^{-6}$ m^2 s^{-1} (at the average water temperature), $\delta = \delta_e$, and the f-parameter in (1) was set to unity. Neither a fully-laminar nor a fully-turbulent boundary-layer profile could be fit successfully to the $Re_C = 17 \times 10^6$ data which suggests a transitional boundary layer at this location and Re_C. These measurements indicate that suction side boundary-layer transition; (i) occurred downstream of $x/C = 0.43$ at $Re_C = 8 \times 10^6$, (ii) was underway but incomplete at $x/C = 0.43$ at $Re_C = 17 \times 10^6$, and (iii) was complete upstream of $x/C = 0.43$ at $Re_C = 33 \times 10^6$. The load-bearing structure of the foil and the LCC precluded velocimetry at other mid-chord locations.

The next nearest downstream location at which boundary-layer profiles could be measured was $x/C = 0.930$. Figure 11 shows the boundary-layer U_t profiles for the suction side (a) and pressure side (b) at this location for the geometry I hydrofoil. To present the data in surface-aligned coordinates, the suction side data measured in vertical profiles at $x/C = 0.930$ and 0.953 have been interpolated to approximate the data along the surface normal at $x/C = 0.930$. For $Re_C = 1.4 \times 10^6$ and 4×10^6, data were not available at $x/C = 0.953$, so the surface normal profile is estimated from the vertical profile using $y \approx h$. A zero velocity point has been added to each profile at the foil surface where neither PIV nor LDV measurements were possible. All the profiles represent turbulent boundary layers and their corresponding fitting parameters are provided in tables 4 and 5 for the suction and pressure sides of the foil, respectively. Here, the f-parameter in (1) and the added degree of freedom provided by $\delta \approx \delta_e$ were used to enhance the smoothness of the profile fits. Also, a vertical coordinate shift within the uncertainty in the LDV's spatial reference was allowed to achieve $B = 5.0$ simultaneously with a best fit to the linear-log region of the boundary-layer profiles. Note that the approximation $y \approx h$ used for the low Re_C data is expected to have a

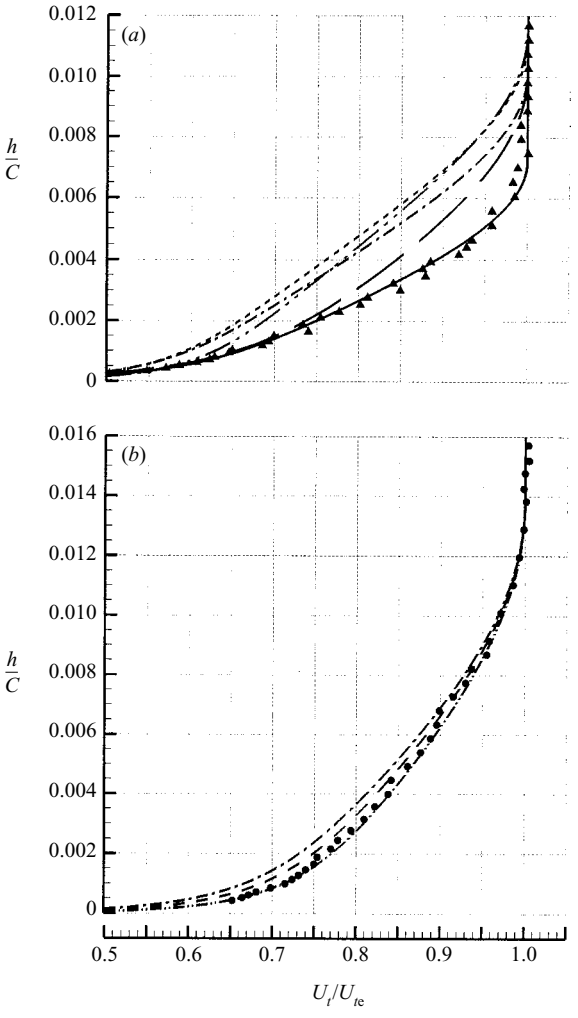

FIGURE 11. Component of the time-averaged velocity tangent to the surface at $x/C = 0.930$ on the (*a*) suction and (*b*) pressure side surfaces of the geometry I hydrofoil. Symbols are measured values. Lines are curve fits using a turbulent boundary-layer profile (as in figure 10) with the fitting parameters provided in tables 4 and 5. For graphical clarity, symbols are shown for only two Re_C. The data scatter at these Re_C is representative of that found at the other Re_C.

Re_C ($\times 10^6$) nominal	U_0 (m s^{-1}) ± 0.01	δ/C ± 0.0002	δ_e^{ps}/δ ± 0.01	U_{te}/U_0 ± 0.01	C_f ± 0.0002	Π ± 0.03	f
8	3.0	0.0140	1.00	0.96	0.0025	0.62	1.15
17	6.0	0.0140	1.00	0.96	0.0023	0.60	1.15
33	12.0	0.0140	1.00	0.96	0.0020	0.60	1.15
50	18.3	0.0140	1.00	0.96	0.0019	0.58	1.16

TABLE 5. Parameters of boundary layers approaching the trailing edge region ($x/C = 0.930$) on the pressure side of the hydrofoil with trailing edge geometry I.

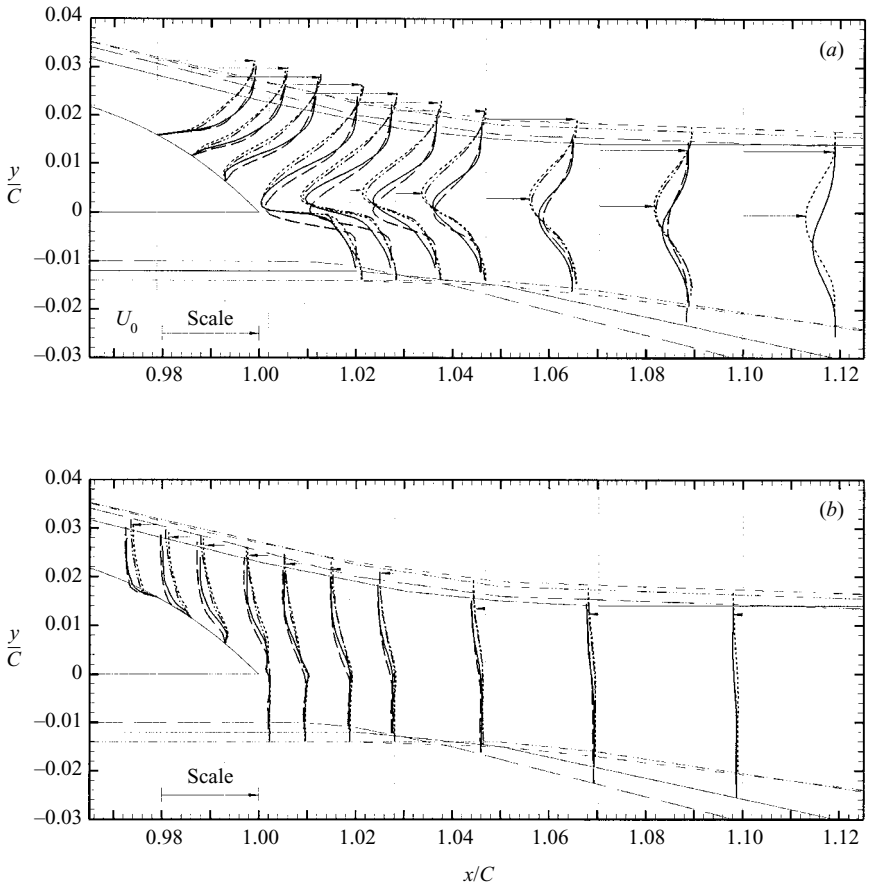

FIGURE 12. The separating boundary layers and near wake with geometry I, presented as the (*a*) streamwise and (*b*) vertical components of the time-averaged velocity, normalized by the velocity far upstream, U_0. The trailing-edge geometry is depicted on the left-hand side of the frame and flow is from left to right. Vertical grey lines are shown at the x/C coordinate of the measurements and provide the axes upon which the velocity values are plotted as black lines. An arrow extends from each axis line to its associated velocity profile. The velocity profiles are plotted within the range $\delta_e^{ps} \leqslant y \leqslant \delta_e^{ss}$, and the field values of δ_e^{ss}/C are δ_e^{ps}/C are shown as thin black lines. The scale used to extract velocity values is provided in the bottom-left corner of the frame. Data at $Re_C = 1.4 \times 10^6$ was not available at the downstream station.

small effect on the boundary-layer fits. As a test case, the same approximation was applied to the $Re_C = 8 \times 10^6$ data, producing a 2% overstatement of Π and negligible effect on the other fitting parameters.

An overview of the mean flow fields near the geometry I and II foil derived from the PIV measurements is provided in figures 12–14. The first two of these figures show multiple velocity profiles of U (figures 12*a* and 13*b*) and V (figures 12*b* and 13*b*) above and downstream of the foil, which is depicted on the left-hand side of each panel. The grey vertical lines indicate the positions at which the profiles were measured. One or two horizontal arrows connect a given flow profile with its measurement location. A relative scale for the flow speeds is given at the lower left-hand side of each panel. The more nearly horizontal curves on each figure indicate the suction-side and pressure-side boundary-layer thicknesses above and below the foil, and the

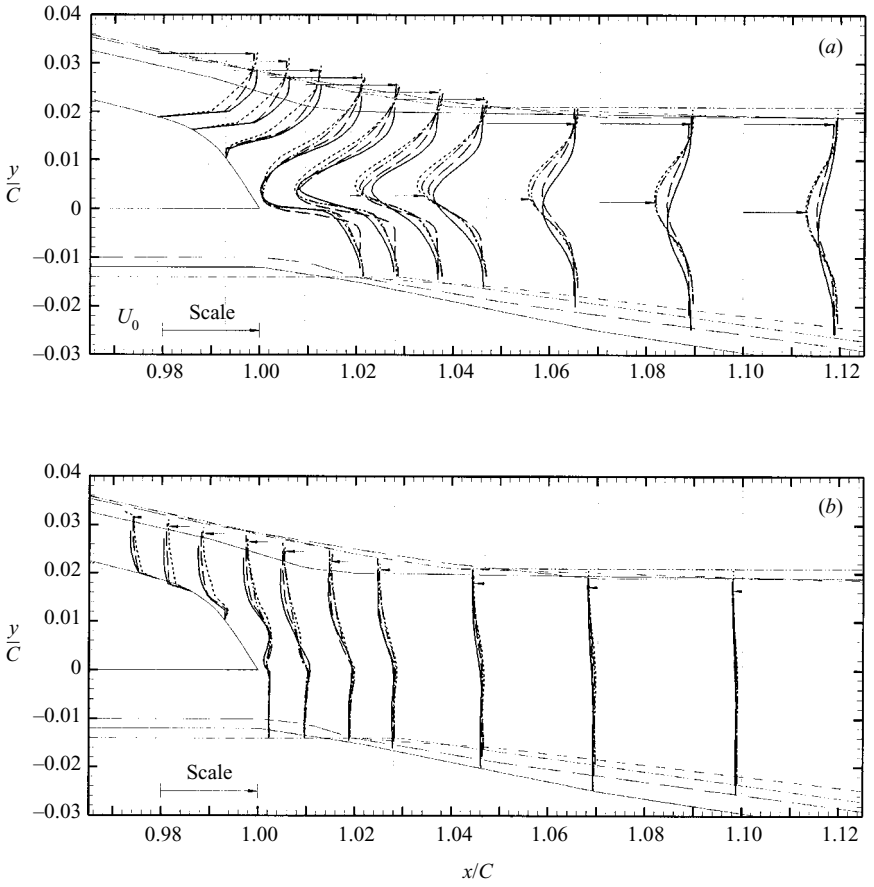

FIGURE 13. The separating boundary layers and near wake with geometry II, presented in the format of figure 12. Data at $Re_C = 50 \times 10^6$ was not available at the three upstream stations.

boundaries of the foil's wake beyond x/C of unity. Excluding $Re_C = 4 \times 10^6$, three general trends are observed: (i) the wake thins as Re_C increases; (ii) the wake is thicker with geometry II; and (iii) the reverse flow region is longer with geometry II. Geometry II at $Re_C = 4 \times 10^6$ is the lone exception to all three of these trends. Figure 14 provides normalized U and V values for geometry I, (*a*), and geometry II, (*b*), at the boundary-layer and wake edges shown on figures 12 and 13. These velocities are used to normalize several of the following plots.

The PIV measurements near the trailing edge and Tecplot® 9.0 software were used to compute apparent stagnation points and separating streamlines. These are shown on figure 15 where arrows indicate flow direction and the interior of closed streamlines are shaded. The apparent stagnation point(s) are marked with black dots, and dashed lines represent streamlines that must exist, but were either not resolved or not recorded within the PIV measurement zone. These streamline patterns are subject to uncertainty from the finite PIV accuracy and from weak, unintended (and unmeasured) spanwise flow, particularly in the recirculation region. In addition, streamlines under the foil could not be determined because shadowing prevented PIV measurements there.

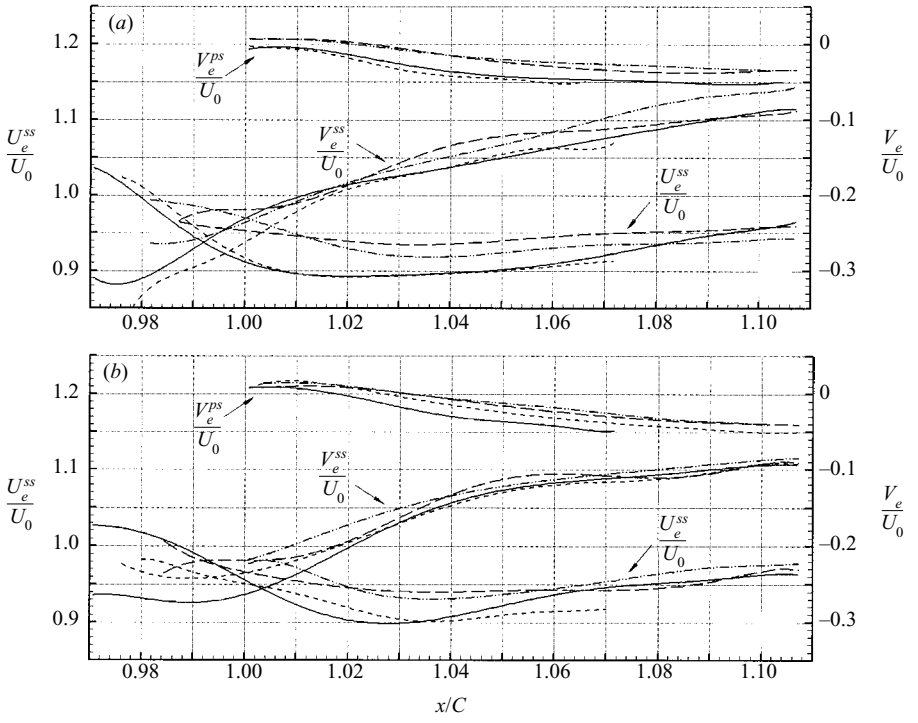

FIGURE 14. Streamwise and vertical components of velocity measured along the field values of δ_e^{ss}/C and δ_e^{ps}/C shown in figures 12 and 13. Panels are for (*a*) geometry I and (*b*) geometry II. Streamwise (vertical) values are read from the axes on the left-hand (right-hand) edge of the panels. Line type indicates Re_C.

Both geometry and *Re*-dependence are apparent in these streamline patterns, with geometry I at $Re_C = 1.4 \times 10^6$ (figure 15*a*) providing a unique case. Here, there is no indication of stagnation or separation at the trailing edge and the streamtube that emerges just below the foil appears to turn upwards without separating from the foil's trailing edge (a complete violation of the Kutta condition), and then flow backwards along the foil surface unit it separates on the suction side. This places an apparent stagnation point just aft of the foil's trailing edge on the lower extent of a detached recirculation zone. However, the volume flux in this contorted streamtube lies at the confidence limits of the PIV measurements. It may be best described as speculative because weak spanwise flow gradients – normal to the PIV plane – might be holding this streamtube open and any spanwise gradient changes might close this streamtube in an orderly fashion. Nevertheless, the $Re_C = 1.4 \times 10^6$ case remains distinguished because the streamline flow-angle farther aft of the foil, which should be much less susceptible to unintended spanwise flow gradients, differs from that shown for the seven other panels of figure 15.

The remaining flow cases (figures 15*b*–15*h*) place a stagnation point at the trailing edge that captures the suction-side separating streamline and launches the dividing streamline into the wake. The suction-side separating streamline encloses a clockwise-rotating recirculation region. Secondary counterclockwise-rotating recirculation regions were found with geometry II (figure 15*e*,*f*). For geometry I, such counterclockwise recirculating regions and associated stagnation points are absent or unresolved.

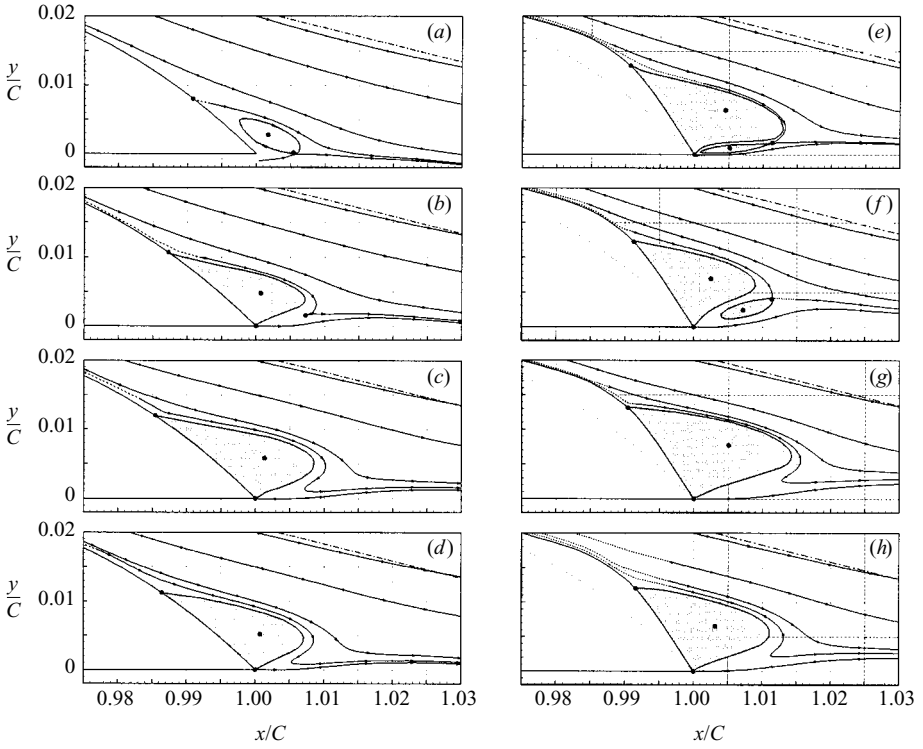

FIGURE 15. Stagnation and separation points and the associated streamlines, derived from the time-averaged velocity fields of the (*a–d*) geometry I and (*e–h*) geometry II: (*a*, *e*) $Re_C = 1.4 \times 10^6$, (*b*, *f*) $Re_C = 4 \times 10^6$, (*c*, *g*) $Re_C = 17 \times 10^6$, (*d*, *h*) $Re_C = 50 \times 10^6$. Separation points are from figure 16(*a*). Stagnation points are those coordinates at which $(U, V) = (0, 0)$. Note that the spanwise velocity was not measured, but is assumed to be negligible based on two-dimensionality. Closed streamlines are filled with grey. Dashed lines indicate sections of streamlines which must exist but are not resolved. The dash-dot line in the upper right-hand corner of each panel runs parallel to the surface tangent at $x/C = 0.930$. Note that for all conditions and geometry, this line approximates the direction of the streamlines for $0.93 < x/C < 1.03$. No data are available for $x/C < 0.993$ at $Re_C = 50 \times 10^6$ for geometry II.

The location of suction side boundary-layer separation was estimated from the data used to create figures 12 and 13 by two methods, and the results appear in figure 16. In the first method, the loci of points at which $U_t = 0$ are plotted in surface-aligned coordinates. Excluding near-wall data contaminated by laser glare and downstream points for which the surface normal has extended into the wake, this loci of points closely approximates a straight line. Taking advantage of this linearity, the loci points for $x/C < 0.998$ and over the ranges $0.0015 < h/C < 0.0050$ and $0.0015 < h/C < 0.0080$ for geometries I and II, respectively, were linearly extrapolated to the surface. This surface point was taken as the zero-velocity separation point, x^U_{sep}. The second method is identical to the first, except that the plotted points are the loci of 50% probability of forward tangential velocity and the extrapolation produces x^γ_{sep}. These two methods would produce identical results in the case of a symmetric probability distribution function for the tangential velocity. However, the results in figure 16(*b*) show that x^U_{sep} is consistently larger than x^γ_{sep} by a small amount. In figure 16(*a*) two results are plotted for geometry I at $Re_C = 8 \times 10^6$ corresponding to

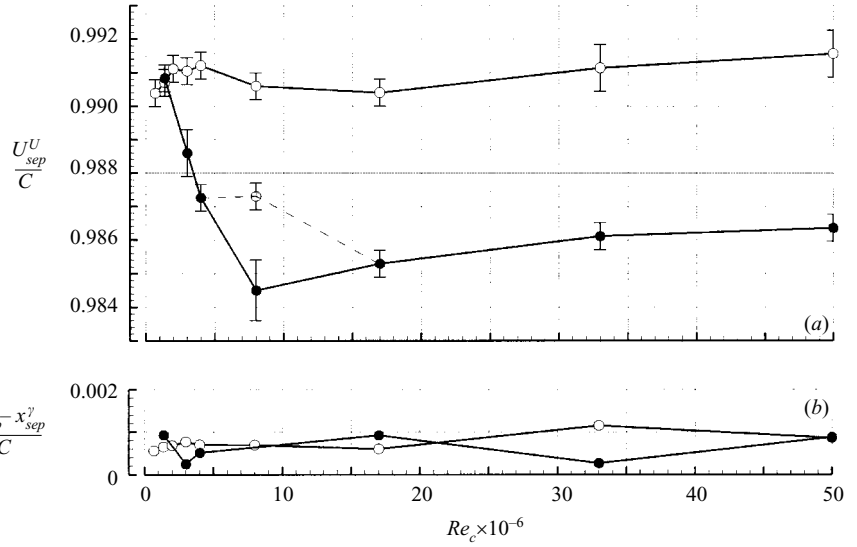

FIGURE 16. The location of separation for both trailing edges at varying Re_C, based on PIV and LDV velocity measurements. Separation was located using two methods: by inflection of the profile of the time-averaged velocity tangent to the surface, U_t, and by probability of forward flow, γ, equal to 50%, where 'forward' is defined by the direction of the surface tangent. Provided are (*a*) results from the first method and (*b*) the difference of the two methods. ●, geometry I; ○, geometry II; ◍, separation at $Re_C = 8 \times 10^6$ for geometry I with delayed suction side boundary-layer transition, discussed in § 3.4.

the two trailing-edge flow fields measured at this condition (see figure 9). The solid dark symbol is for the thicker wake that is consistent with the LDV measurements.

In figure 16(*a*), the two trailing-edge geometries show similar trends of suction side separation with Re_C for $Re_C > 8 \times 10^6$. However, as Re_C decreases below 8×10^6, suction side separation on geometry I moves rapidly downstream, while separation on geometry II is roughly constant. This behaviour is attributed to differences in boundary-layer separation on the pressure side. At the lowest Re_C values, the pressure side boundary layer is laminar or transitional when it reaches the trailing edge, while the suction side boundary layer is turbulent. As these boundary layers evolve downstream and encounter an increasingly adverse pressure gradient at the trailing edge, the laminar pressure side boundary layer thickens more quickly than the turbulent suction side layer, and is believed to detach prior to the trailing edge. On geometry I, the suction side boundary layer is then able to advance further downstream. The geometry II edge sees a similar competition between its laminar pressure side and turbulent suction side boundary layers, but the steep trailing-edge bevel prevents the suction side from advancing further downstream. As a result, the pressure side boundary layer remains attached. Early pressure side separation on geometry I provides an explanation not only for figure 16, but also for the unique appearance of panel (*a*) among the other panels of figure 15.

The evolution of the suction side boundary layer across separation for both trailing edges, is provided in figure 17 at $x/C = 0.930$, 0.979, 0.998 and 1.028 and $Re_C = 1.4 \times 10^6$, 4×10^6, 8×10^6 and 50×10^6. Here, the trailing-edge coordinate frame (a fixed rotated Cartesian coordinate system defined by h and t at 93% chord) is used to determine the U_t profiles at each x/C value. This coordinate system, which

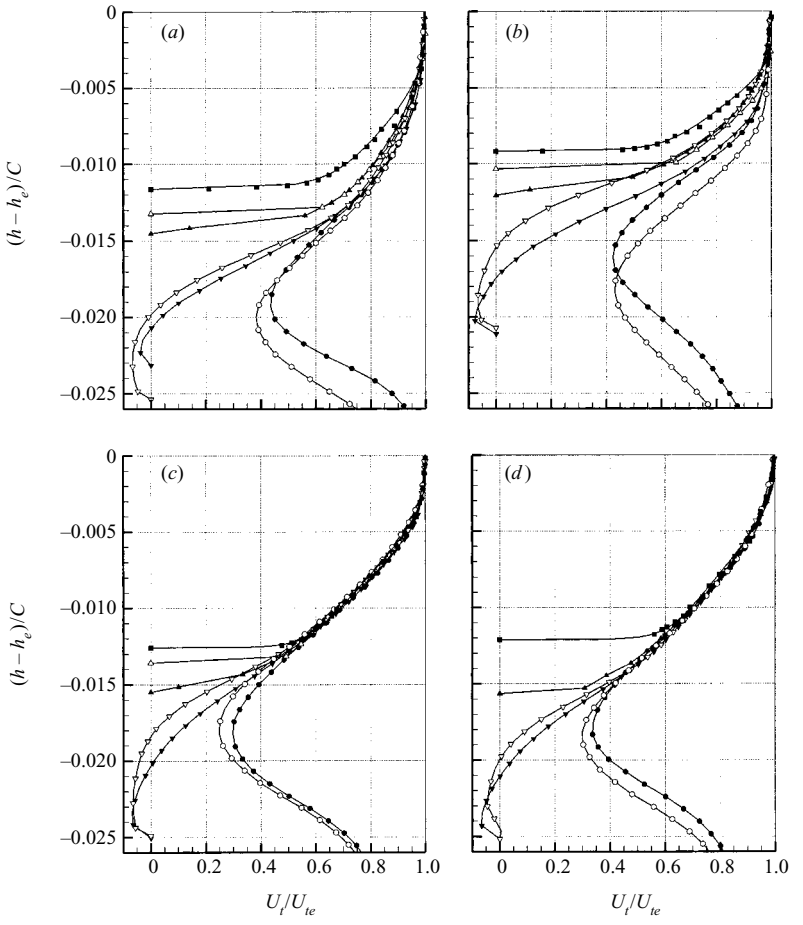

FIGURE 17. The time-averaged velocity profiles across separation, at varying Re_C for both trailing edges. The profiles are presented in a rotated Cartesian coordinate frame aligned to the surface tangent at $x/C = 0.930$. To best collapse the profiles, the spatial coordinate has been shifted by the boundary-layer thickness, δ_e^{ss}, measured in the rotated frame and designated h_e. Presented are measurements at (*a*) $Re_C = 1.4 \times 10^6$, (*b*) $Re_C = 4 \times 10^6$, (*c*) $Re_C = 17 \times 10^6$ and (*d*) $Re_C = 50 \times 10^6$. Closed symbols are for geometry I, while open symbols are for geometry II at varying x/C: ■, $x/C = 0.930$; ▲, $x/C = 0.979$; ▼, $x/C = 0.998$; ●, $x/C = 1.028$. No data are available for $x/C = 0.979$ at $Re_C = 50 \times 10^6$ for geometry II.

is rotated $\beta = 14.12°$ from the (x, y) system, was chosen because it approximates a streamline coordinate system for all flow conditions in the region $0.930 < x/C < 1.028$. The U_t profiles are also vertically aligned to match at h_e, the location of the boundary-layer edge or near-wake edge in the 93%-chord Cartesian frame. The data show that the thinnest boundary layers occur at $Re_C = 4 \times 10^6$, and that the outer part of the boundary-layer flow evolves more rapidly at the lower two values of Re_C than at the higher two. In fact, at the higher two Re_C values, the outer part of the boundary layers (when normalized by the local external velocity) appears to be insensitive in the presence or absence of the foil surface. Under this velocity normalization and coordinate frame, the outer portion of the attached boundary layers crosses separation with little change, and the *Re*-dependence of the attached boundary layers sets the *Re*-dependence of the initial wake.

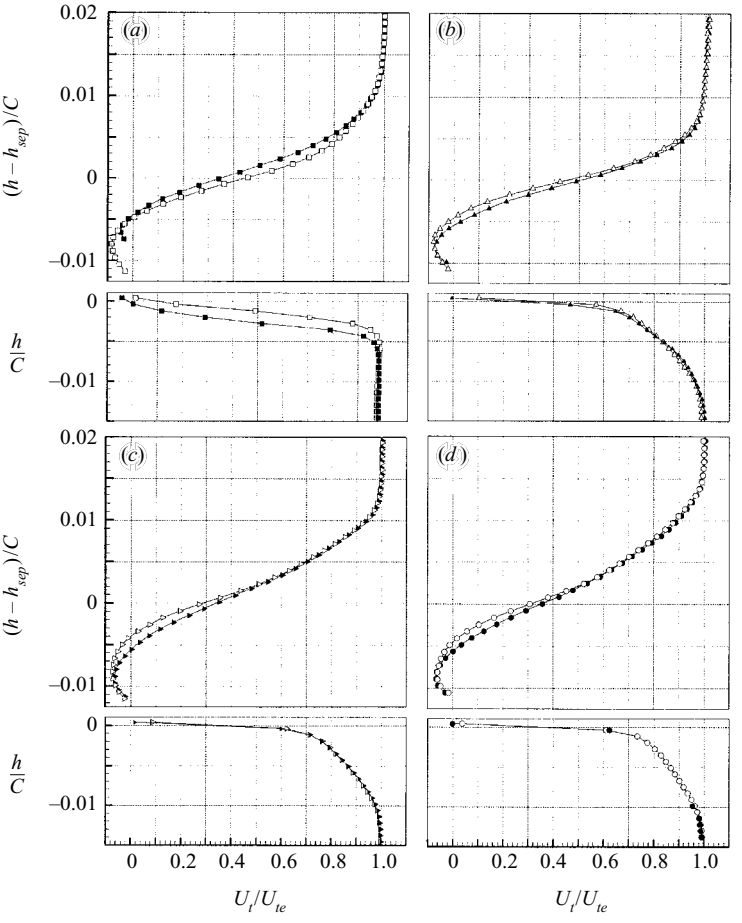

FIGURE 18. The time-averaged velocity profiles for both trailing edges at varying Re_C. Suction side data are from $x/C = 1$. Owing to the shadow of the foil, pressure side data was not available at this coordinate, and so data at $x/C = 1.002$ are presented. The suction (pressure) side data are presented in a rotated Cartesian coordinate frame, aligned to the suction (pressure) side surface tangent at $x/C = 0.930$. To best collapse the geometry dependence of the flow, the spatial coordinate of the suction side data is shifted by the thickness of the trailing edge at the separation point, measured in the rotated frame and designated h_{sep}. No shift is applied to the pressure side data. Presented are measurements at (*a*) $Re_C = 1.4 \times 10^6$, (*b*) $Re_C = 4 \times 10^6$, (*c*) $Re_C = 17 \times 10^6$, and (*d*) $Re_C = 50 \times 10^6$. Closed symbols are for geometry I, while open symbols are for geometry II. Data at $Re_C = 50 \times 10^6$ for geometry I are incomplete owing to shadowing, but by all indications collapses with the data from geometry II.

This geometry dependence is explored more fully in figure 18 which shows trailing-edge profiles of U_t at $Re_C = 1.4 \times 10^6$, 4×10^6, 17×10^6 and 50×10^6 from the suction side at $x/C = 1.000$ and the pressure side at $x/C = 1.002$. Here the suction side results are again plotted in the trailing-edge coordinate frame, but the profiles are now vertically aligned by the h-coordinate of the foil surface at suction side separation, h_{sep}. The pressure side profiles simply present U plotted in the (x, y)-coordinates frame. (On the pressure side $U = U_t$ and $y_{sep} = 0$, so figure 18 actually presents the pressure and suction side results on an equal footing.) The normalizing velocities can be derived from the data on figure 14. The three higher Re_C values show good profile agreement on the pressure side and on the suction side for $h - h_{sep} > 0$. Thus, the

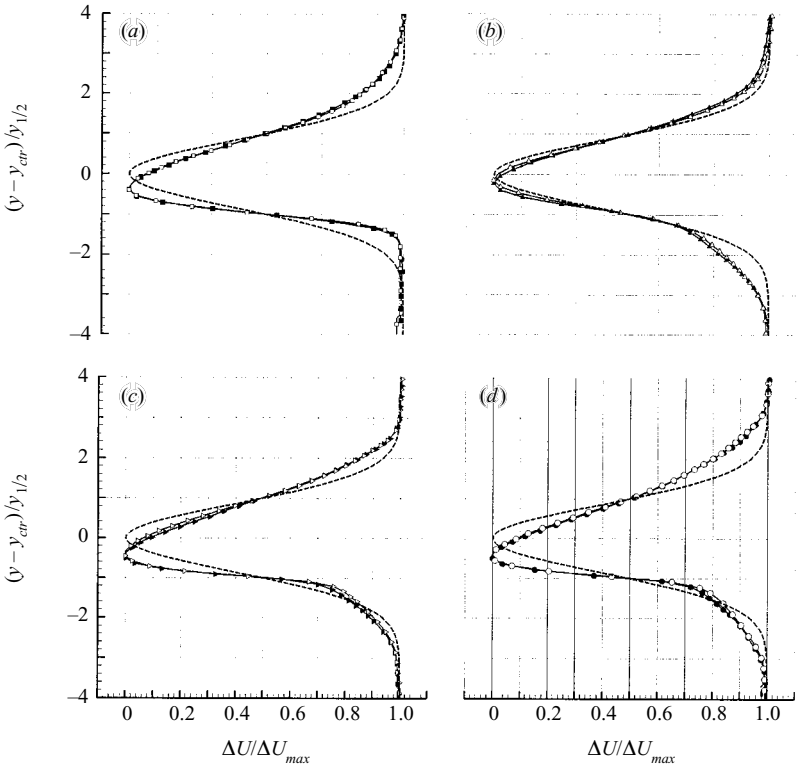

FIGURE 19. Time-averaged streamwise velocity profiles at $x/C = 1.0094$, for both the trailing edges. Panels show results at (*a*) $Re_C = 1.4 \times 10^6$, (*b*) $Re_C = 4 \times 10^6$, (*c*) $Re_C = 17 \times 10^6$, and (*d*) $Re_C = 50 \times 10^6$. Symbols give measured values and the dashed line gives the Gaussian fit matched at the half-width points. Closed symbols are for geometry I, while open symbols are for geometry II.

main geometric effect of the trailing-edge modification on the wake is communicated through the suction side separation point. The $Re_C = 1.4 \times 10^6$ case does not fit this geometrical trend because the pressure side boundary layer separates prior to the trailing edge on geometry I and at the trailing edge on geometry II. Therefore, a shift accounting only for suction side separation does not collapse the geometry dependence at this Re_C.

The flow profiles that appear in figure 18 initiate the foil's wake. Figures 19, 20 and 21 show the subsequent flow evolution in (x, y)-coordinates at $x/C = 1.009$, 1.028 and 1.047, respectively, for $Re_C = 1.4 \times 10^6$, 4×10^6, 17×10^6 and 50×10^6. Here, the flow has been scaled as a plane wake; the horizontal axes are $\Delta U/\Delta U_{max}$ where $\Delta U = U - U_e^{ss}$, and the vertical axes are $(y - y_{ctr})/y_{1/2}$ where y_{ctr} denotes the average of the vertical coordinates corresponding to $\Delta U = \Delta U_{max}/2$, and $2y_{1/2}$ is the full wake width where $\Delta U = \Delta U_{max}/2$. On each frame of figures 19–21, a Gaussian profile, matched at the half-width points, is plotted to indicate the extent of wake convergence to a standard symmetrical form. In figure 19 ($x/C = 1.009$), every profile shows some skewness as a remnant of the foil boundary layers' asymmetry, with $Re_C = 4 \times 10^6$ being the most symmetrical. In figure 20 ($x/C = 1.028$), the profile skewness is reduced in every case and is nearly absent at $Re_C = 4 \times 10^6$. On figure 21, the various wakes have relaxed to a self-similar Gaussian profile and subsequent wake evolution involves little or no further profile shape changes.

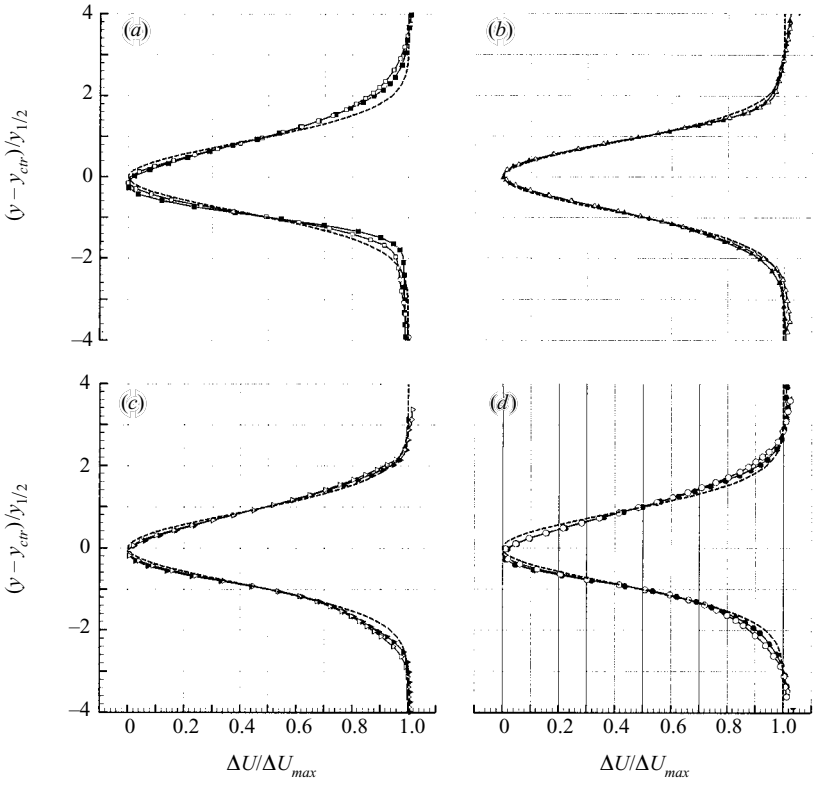

FIGURE 20. Time-averaged streamwise velocity profiles at $x/C = 1.0281$, for both trailing edges, in the format of figure 19.

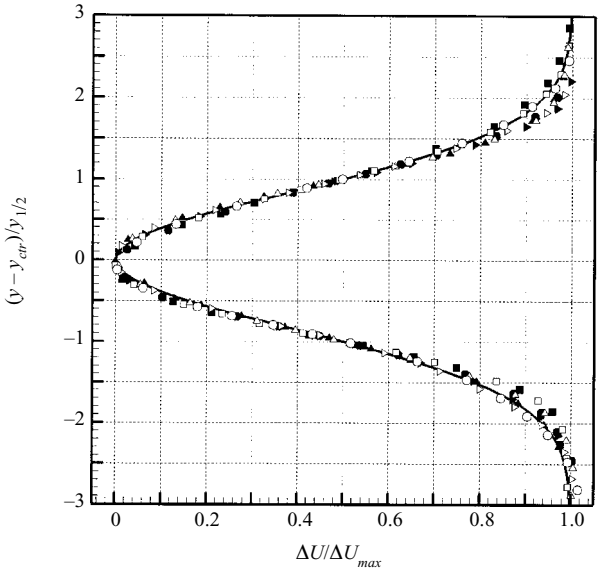

FIGURE 21. Time-averaged streamwise velocity profiles at $x/C = 1.0469$, for both trailing edges at $Re_C = 1.4 \times 10^6$, 4×10^6, 17×10^6 and 50×10^6. Symbols give measured values and the solid line gives a Gaussian fit. Closed symbols are for geometry I, while open symbols are for geometry II.

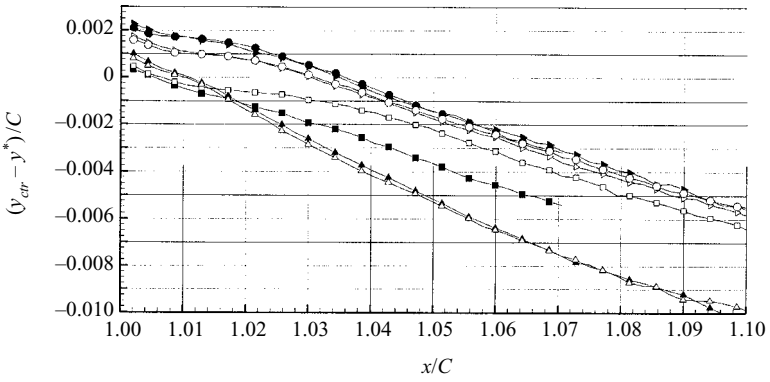

FIGURE 22. The wake profile centre coordinate, y_{ctr}/C, used in figures 19–21 and plotted against x/C for varying Re_C for both trailing edges. For all Re_C shown except 1.4×10^6, a collapse of the geometry-dependence of this parameter is achieved by shifting y_{ctr} by an amount, y^*, derived from the hydrofoil thickness at the separation point. The lack of collapse at $Re_C = 1.4 \times 10^6$ is due to the variation with geometry of pressure side separation. Closed symbols are for geometry I, while open symbols are for geometry II.

Given the similarities shown on figures 19–21, wake flow differences can be readily assessed by examining how y_{ctr}, ΔU_{max} and $y_{1/2}$ evolve downstream of the foil. The first of these is shown in figure 22 where $(y_{ctr} - y^*)/C$ is plotted *vs.* x/C. Here, the value of y^* is the vertical increment obtained by extrapolating the foil thickness at suction side separation downstream to the trailing edge along a line parallel to the t-axis of the 93%-chord rotated Cartesian system: $y^* = (1.0 - x^U_{sep}/C)\tan\beta$. This vertical shift nearly collapses the wake centre results for the two trailing-edge shapes at each Re_C except for $Re_C = 1.4 \times 10^6$. This further confirms that the main impact of the differing trailing edges on the foil's mean flow can be accounted for with a vertical shift related to suction side separation. As mentioned earlier, the $Re_C = 1.4 \times 10^6$ case involves early pressure side separation and a shift based on suction side separation is insufficient to collapse the geometry dependence.

The downstream evolution of the wake velocity deficit, ΔU_{max}, is shown in figure 23 for both trailing edges at $Re_C = 1.4 \times 10^6$, 4×10^6, 17×10^6 and 50×10^6. As before, the normalizing velocity U_e^{ss} is extracted from the data in figure 14. The curves are downward trending as expected, and the strongest Reynolds-number variation reveals a pairing of the two higher Re_C and the two lower Re_C. Finally, the downstream evolution of the wake half width, $y_{1/2}$, is shown in figure 24 for both trailing edges with the same four Re_C. The curves are upward trending as expected, and there is substantial Reynolds number variation. In particular, at $Re_C = 4 \times 10^6$ with geometry II, the wake leaves the trailing edge as the thinnest, but by 10% of chord downstream it has become the thickest, and this growth rate is not matched or exceeded by the flow at any other Reynolds number.

4. Discussion

The data presented above indicate that the flow near the trailing edge and in the near wake changes with both Reynolds number and trailing-edge geometry. These changes can be related to the state of the suction and pressure side boundary layers upstream of the trailing-edge separation. Here, a combination of laminar and

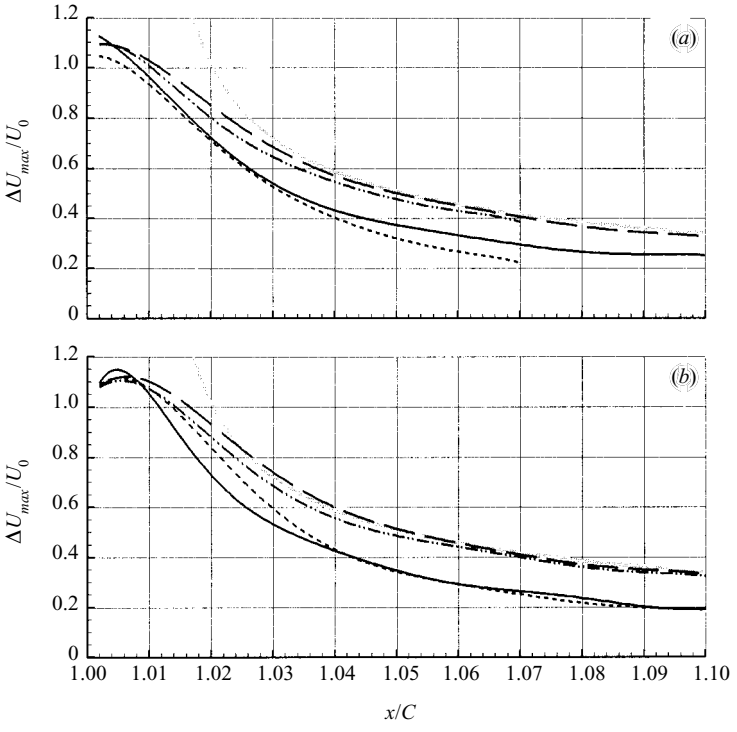

FIGURE 23. The wake velocity deficit used in figures 19–21, plotted against x/C for varying Re_C and for (*a*) geometry I and (*b*) geometry II. The black lines are polynomial fits of the measured values. The solid grey line is the wake scaling law of Sreenivasan & Narasimha (1982), using the momentum thickness of the far wake and $x/C = 1.01$ as the hypothetical origin of the wake.

turbulent boundary-layer integral calculations were used to infer transition location, shape factor $H = \delta^*/\theta$, and momentum thickness θ for the two boundary layers where direct measurements of these flow parameters were not possible. Here, the usual definitions of δ^* and θ apply:

$$\delta^* = \int_{h=0}^{h=\delta_e} \left(1 - \frac{U_t}{U_{te}}\right) \mathrm{d}h, \tag{2}$$

$$\theta = \int_{h=0}^{h=\delta_e} \frac{U_t}{U_{te}} \left(1 - \frac{U_t}{U_{te}}\right) \mathrm{d}h. \tag{3}$$

4.1. *Boundary-layer transition on the hydrofoil*

First, the averaged pressure distribution (average of all Re_C and geometries) on the hydrofoil and Thwaites' method (see White 1991) were used to compute the growth of the laminar boundary layer from the leading-edge stagnation point to the region of boundary-layer transition. The one-step method of Michel (1952, see White 1991) was then used to predict the location of boundary-layer transition. The results of

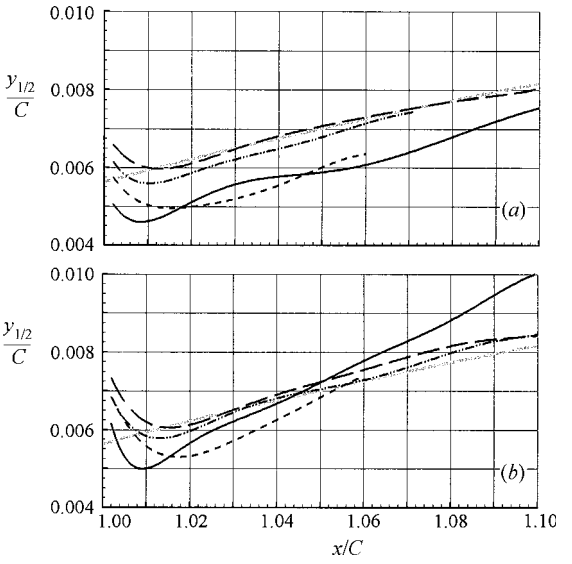

FIGURE 24. The wake half width used in figures 19–21, plotted against x/C for varying Re_C and for (*a*) geometry I and (*b*) geometry II. The black lines are polynomial fits of the measured values. The solid grey line is the wake scaling law of Sreenivasan & Narasimha (1982), using the momentum thickness of the far wake and $x/C = 0.91$ as the hypothetical origin of the wake.

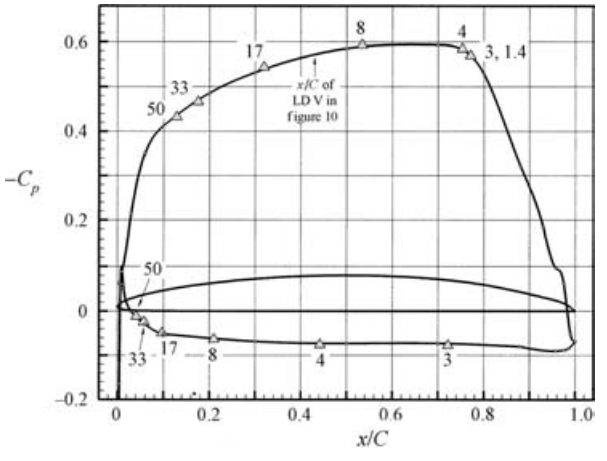

FIGURE 25. Location of boundary-layer transition, predicted from the mean C_p curve using Thwaites' method and the one-step method of Michel (1952). ○, measured C_p value; ——, spline of C_p values; △, predicted transition location at the Re_C (in millions) indicated.

these calculations are depicted in figure 25 against the speed-averaged-C_p curves. The calculated location of transition on both sides of the foil moves upstream with increasing Re_C. For Re_C below 4×10^6, the flow on the suction side is computed to remain laminar until the steep adverse pressure gradient beginning at $x/C \sim 0.7$. These calculations are confirmed, where data is available, by the LDV-measured velocity profiles from $x/C = 0.43$ (figure 10). These profiles suggest that transition moved upstream of $x/C = 0.43$ between Re_C of 8×10^6 and 17×10^6.

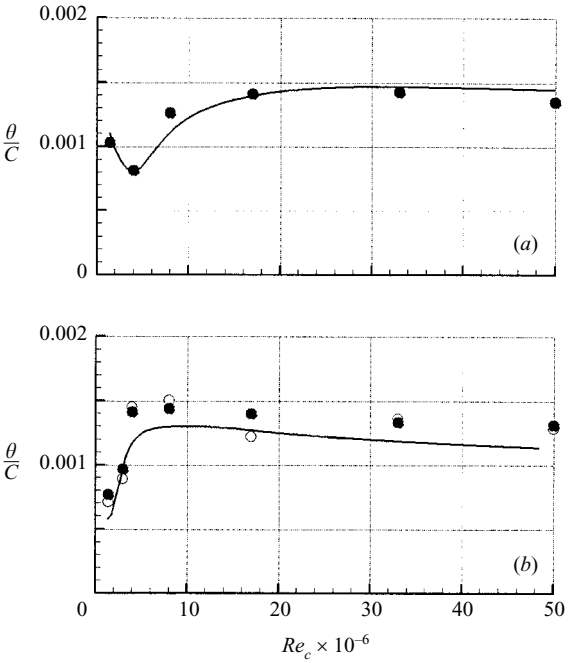

FIGURE 26. Measured and predicted boundary-layer momentum thickness, θ, at varying Re_C. (*a*) Thickness of the suction side boundary layers for geometry I at $x/C = 0.930$, shown in figure 10. (*b*) Thickness of the pressure side boundary layers for both trailing edges at $x/C = 1$. Where available (geometry I, Re_C of 8×10^6 and above), the values are computed from LDV measurements at $x/C = 1$. Otherwise, the values are computed from the wake data at $x/C = 1.002$ shown in figure 18; ●, computed from data from geometry I; ○, computed from data from geometry II; ——, prediction from the boundary-layer integral methods.

4.2. *Boundary layers approaching TE region*

The boundary-layer parameters obtained from the Thwaites method at the Michel-predicted transition point were employed as initial values for a turbulent boundary-layer integral calculation (White 1991). The momentum thickness was assumed continuous across the calculated transition point. Of course, actual boundary-layer transition occurs over a finite region so the computed results obtained here are approximate in this regard. The turbulent boundary-layer calculations were not used for the pressure side boundary layer below $Re_C = 3 \times 10^6$ because the PIV results at $x/C = 1$ revealed a laminar or transitional boundary layer leaving the trailing edge on the pressure side. At these conditions, a transition location was not calculated, and the Thwaites method was used exclusively.

A sample of the outcome of these calculations is shown in figure 26 where the predicted and measured suction- and pressure-side boundary-layer momentum thicknesses, θ, at $x/C = 0.93$ are plotted *vs.* Re_C for geometry I. Considering the approximate nature of the analysis, the agreement between the calculations and measurements is good. For the suction side, the location of transition is roughly fixed at Re_C below 4×10^6 (see figure 28). As a result, as Re_C increases from the lowest values to $Re_C = 4 \times 10^6$, θ decreases owing to boundary-layer thinning with increasing Re_C. However, as Re_C increases above 4×10^6, the transition point begins to move upstream and increases the turbulent development length of the boundary layer. Thus, θ increases with increasing Re_C for $Re_C > 4 \times 10^6$. As a result, $Re_C = 4 \times 10^6$ produces

a minimum in the suction side boundary-layer thickness. The *Re*-dependence of the pressure side boundary-layer thickness is due to similar effects, but without a fixed transition point. In this case, $Re_C = 4 \times 10^6$ corresponds roughly to a maximum in the pressure side boundary-layer thickness.

The success of these boundary-layer calculations has implications concerning the *Re* and geometry dependence of the hydrofoil flow. Since the evolution of θ with increasing x/C is predicted well by a single C_p distribution, the *Re* and geometry dependence of the potential flow must have a weak influence on boundary-layer development. This means that the upstream feedback from separation and the wake does not appreciably affect the state of the attached boundary layers. Instead, the character of these attached boundary layers is derived primarily from the *Re*-dependence of transition and its effect on the laminar and turbulent boundary-layer development. This claim is made more significant by the finding of figure 17, which shows the *Re*-dependence of the outer portions of the attached boundary layers crossing separation with little change. This behaviour, as well as other aspects of separation and the near wake will be discussed in the following section.

4.3. *Separating boundary layers and initial wake*

This section discusses the more complex *Re* and geometry dependence of the flow nearest to the trailing edge. In this region, the boundary layers at $x/C = 0.93$ further evolve to separate and form the near wake. On the suction side of the foil aft of $x/C = 0.93$, a steep adverse pressure gradient leads to boundary-layer separation and the boundary-layer integral methods lose validity. However, suction side boundary-layer integral quantities are still expected to exhibit some similarities. As discussed in Simpson (1989), boundary layers near separation exhibit a relationship between a simple function of the shape factor, $\tilde{h} = (H-1)/H$, and the ratio δ^*/δ_e. Figure 27 presents these two quantities for the separating suction side boundary layers on both trailing edges along with correlations developed from backward facing steps, $\tilde{h} = 1.5(\delta^*/\delta_e)$ and power-law profiles, $\tilde{h} = (2-\delta^*/\delta_e)^{-1}$ (see Simpson 1989). The intersection of these two correlations indicates the point of intermittent boundary-layer detachment on a flat-plate. Here, H and δ^*/δ_e are computed from U_t in surface-aligned coordinates, and the data plotted range from $x^{\gamma}_{sep}/C - 0.004 \leqslant x/C \leqslant x^{\gamma}_{sep}/C + 0.011$ for geometry I and $x^{\gamma}_{sep}/C - 0.003 \leqslant x/C \leqslant x^{\gamma}_{sep}/C + 0.003$ for geometry II. The open symbols in figure 27(*a*) and the filled symbols in figure 27(*b*) for each flow condition correspond to the boundary-layer state at 50% probability of forward flow.

For surfaces of low curvature and pressure gradient, the paths of the boundary layers in the vicinity of separation are roughly linear and collapse on the line of slope 1.5 indicated in figure 27. Several of the data sets presented here have linear regions with this slope, but the overall collapse to a single line is imperfect, as might be expected for the curved-surface foil boundary-layer flows of this study. However, figure 27 does reveal a relationship between boundary-layer integral quantities at separation, and demonstrates both Re_C and geometry dependence in the flow. The Re_C dependence is apparent in the variation between paths at different values of Re_C. In particular, the $Re_C = 4 \times 10^6$ data generally lie above the plotted points for the other Re_C values. Trailing-edge geometry dependence is apparent in the grouping of the data, with the geometry I results (figure 27*a*) lying above the geometry II results (figure 27*b*). This places the higher surface curvature results from geometry II further from the flat-plate results. The extreme case of high surface curvature at separation is achieved by the foil's separating pressure side boundary layer where $H \approx 1.3$ (as expected, see Schlichting 1979).

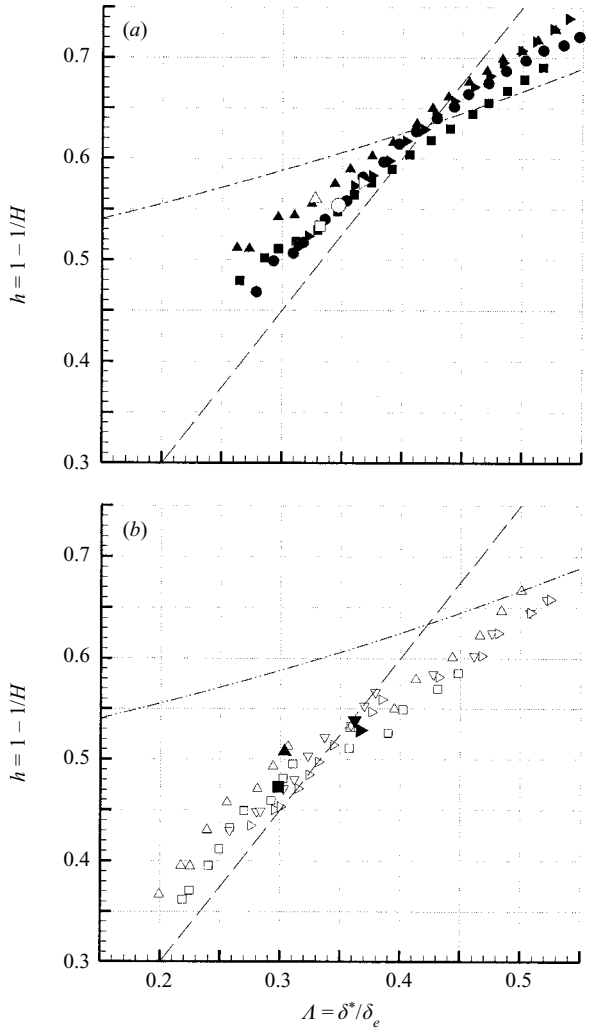

FIGURE 27. Boundary-layer parameters associated with separation for (*a*) geometry I and (*b*) geometry II at varying Re_C. Symbols give the boundary-layer state derived from PIV measurements. The boundary layer state at the separation point (from figure 16*a*) is plotted as a symbol with inverse fill. Lines provide the fits (see Simpson 1989): — — —, correlation for boundary layers separating from flat plates and steps; — ·· —, probability of forward flow, $\gamma = 0.8$ on flat plates and steps.

The data presented in figure 17 also show that when a turbulent boundary layer separates from a rapidly curving surface, there is a lag in the communication of the near-wall changes to the outer flow, a finding that is similar to that of Morris & Foss (2001). In particular, above $Re_C = 17 \times 10^6$, the momentum-containing portions of the separated boundary layers at the trailing edge, $x/C = 1.0$ are essentially the same as the outer portions of the attached boundary layers at $x/C \approx 0.98$ (when normalized by the local free stream). In addition, the trailing-edge geometry dependence of the suction-side boundary-layer flow as it leaves the foil appears to be determined by the location of the suction side separation point for $Re_C \geqslant 4 \times 10^6$. In the trailing-edge coordinate frame (93% chord Cartesian coordinates), the suction-side U_t profiles for

$(h-h_{sep})/C>0$ are essentially identical between the two geometries, at least at the higher three Reynolds numbers, and the primary flow-field variations are confined to $(h-h_{sep})/C<0$ (figure 18).

On the pressure side of the foil beyond $x/C=0.93$, the boundary-layer development story is much simpler. Here, the pressure side boundary layers encounter a mildly adverse pressure gradient as x/C increases toward unity. In the absence of this pressure gradient, separation is expected at the trailing edge. Pressure-side boundary-layer profile measurements made for $0.93\leqslant x/C\leqslant 1$ are limited to geometry I at Re_C of 8×10^6, 17×10^6, 33×10^6 and 50×10^6. Results for geometry II at these Re_C values were expected to be nearly identical between geometries because of their similar static pressure distributions (see figures 3 and 4). All pressure-side velocity profiles are very similar to flat-plate results, the displacement and momentum thickness vary according to established correlations, and skin friction coefficients inferred from the pressure side velocity profiles agree well with the Schultz–Grunow correlation (see Schlichting 1979). Although pressure side boundary-layer profiles were not recorded for Re_C below 8×10^6, the initial wake velocity profiles from $x/C=1.002$ (figure 18) retain the character of the pressure side boundary-layer. With the exception of geometry I at $Re_C=1.4\times10^6$, these nearest-wake profiles suggest pressure-side boundary-layer separation occurs at the trailing edge.

4.4. *Development of the wake*

As the near wake of the foil converts to a far wake, its characteristics should trend toward those of an ideal two-dimensional wake with a constant momentum thickness. Here, the momentum thickness, θ_w of the foil's wake is defined by

$$\theta_w=\int_{y=-\delta_{e,ps}}^{y=\delta_{e,ss}}\frac{U(y)}{U_e}\left(1-\frac{U(y)}{U_e}\right)\mathrm{d}y, \tag{4}$$

where δ_e^{ps} and δ_e^{ss} are defined by the vertical locations where $U=U_e^{ss}$. The geometry I LDV profiles in figure 8 were used to calculate an average momentum thickness for the far wake at $Re_C=8\times10^6$ to 50×10^6, $\theta_w/C=0.0039$. Because of the difficulty in defining δ_e^{ps} and δ_e^{ss}, the uncertainty in θ_w is high and as Re-specific calculation is not justified. The wake-center velocity deficit, ΔU_{max}, and half-width $y_{1/2}$, were then estimated from the wake scaling laws in Sreenivasan & Narasimha (1982): $\Delta U_{max}/U_0\approx1.63[\theta/(x-x_0)]^{1/2}$ and $y_{1/2}\approx0.30[(x-x_0)\theta]^{1/2}$, where x_0 is a hypothetical origin of the wake. These scaling relationships are plotted in figures 23(a) and 24(a), where x_0/C is selected for a best fit and is 1.01 for the scaling of ΔU_{max} and 0.91 for the scaling of $y_{1/2}$. The same values for x_0 and θ_w (we lack far wake data for geometry II) are used to produce the curves in figures 23(b) and 24(b). Although the match to the measured data is better for the wake velocity deficit ΔU_{max}, the wake scaling laws appear reasonably successful for the higher Re_C flows beyond $x/C=1.03$.

Overall, the foil's wake flow changes little from Re_C of 8×10^6 to 50×10^6, but the findings at $Re_C\leqslant4\times10^6$ show much more variability. For example, the wake profile at $Re_C=4\times10^6$ for both trailing edges relaxes to near-perfect Gaussian form closest to the trailing edge when compared to the wake profiles at the other Re_C (see figures 19 and 20). These observations suggest there is augmented turbulent transport occurring in the foil's near wake at $Re_C=4\times10^6$. This contention is supported by the observation of vortex shedding fluctuations in the foil's near wake at this Re_C. Additional discussion of vortex shedding is deferred to a future paper on this topic.

4.5. *Hydrofoil lift and drag*

The overall suite of measurements is sufficient to allow the calculation of the foil's lift and drag by two nearly independent methods for geometry I. With geometry II, only one of these methods was viable. These calculations were undertaken to establish foil performance and to validate the internal consistency of the measurements made with geometry I. Here, lift and drag are reported as the two-dimensional lift and drag coefficients (C_L and C_D) with the foil chord C used as the length scale in both cases.

The first method involved integrating the foil's surface stresses to determine foil lift and drag. The input data here were the splined pressure distributions and the skin-friction stress calculated from the boundary-layer integral analysis. From this method, C_L for geometry I was determined to vary approximately linearly with Re_C from 0.52 to 0.55 ± 0.01 for Re_C between 8×10^6 and 50×10^6, and C_L for geometry II was determined to be 0.52 ± 0.01 and constant within the given uncertainty for the same range of Re_C. Here, C_D was found to be 0.006 ± 0.001 and constant with Re_C within the given uncertainty for both trailing-edge geometries. In all cases, approximately 60% of the total drag originated from skin friction, and 40% from pressure. The uncertainty in lift is derived from that of the static pressure measurements, discussed earlier. For the drag calculations, the dominant source of uncertainty is the skin friction values predicted using the boundary-layer integral method. This uncertainty is estimated at $\pm 20\%$ by comparing the predicted C_f values to those derived from the linear-log region of the measured velocity profiles at $x/C = 0.93$.

The second method employed a two-dimensional rectangular control volume enclosing the hydrofoil flow and defined by the corner coordinates $(x/C, y/C) =$ $(-1.25, -0.19)$, $(-1.25, 0.26)$, $(1.43, 0.26)$ and $(1.43, -0.19)$. A uniform inflow velocity and the LDV far-wake survey data (figure 8) were used as velocity boundary conditions on the upstream and downstream control surfaces. Wall static pressure (figure 5) confirmed that the upstream pressure is uniform, but showed that the pressure in the far wake location was not. Therefore, the steady incompressible Bernoulli equation was used to provide the pressure on the downstream control surface, with the exception of the region of the wake where measured velocity fluctuations are substantial ($-0.07 < y/C < 0.05$). Here, linear interpolation between the Bernoulli-derived pressures was used. The splined test section wall static pressures, including the interpolated value on the suction side at $x/C = 0.7$ (figure 5), were used to provide the pressure boundary conditions on the upper and lower control surfaces. Again, the Bernoulli equation was used to determine flow velocity magnitudes along this surface. The assumed pure horizontal inflow direction, and the measured flow directions at the leading edge, at the trailing edge, and in the far wake were then linearly interpolated to provide a continuous estimate of the flow direction along the upper and lower control surfaces. Lift and drag contributions from turbulent fluxes were not included. These control volume calculations were undertaken for $Re_C = 8 \times 10^6$, 17×10^6, 33×10^6 and 50×10^6. The imbalance in mass conservation over this range of Re_C, for the control volume described, was no greater than $\pm 0.1\%$ of the mass flux at the inflow surface. This result is sensitive to the interpolation scheme used to provide the flow direction on the upper and lower surfaces, as well as the calibration uncertainty in the LDV measurements.

From this second method, C_L for geometry I was found to be 0.55 ± 0.05, with Re_C variation falling within this larger uncertainty. The greatest source of this uncertainty is the interpolated value of the wall static pressure at $x/C = 0.7$ used on the upper control surface. Here, the foil's C_D was found to be 0.009 ± 0.003, with Re_C variation again falling within the uncertainty. For the drag calculations, the greatest source of

uncertainty is the $\pm 1\%$ calibration uncertainty in the LDV, exacerbated by the use of separate LDV systems for the inflow and far wake data acquisition. The upper and lower control surface approximations have minimal effect on the drag calculations. Most significantly though, the two methods for calculating lift and drag coefficients for the geometry I foil, produced results that agree within uncertainty.

5. Summary and conclusions

The mean flow around a large two-dimensional hydrofoil has been experimentally investigated with special attention given to the separated flow near its bevelled trailing edge. Two trailing-edge shapes were investigated that are of interest for practical applications. The data reported here are unique because of the high Reynolds numbers attained. This effort leads to four conclusions.

First of all, over the range of chord-based Reynolds number from 1.4×10^6 to 50×10^6, and for the geometries tested, the Reynolds number and geometric dependencies of the flow field are mild, but clearly measurable. The majority of the observed Reynolds-number dependence comes from the development of the attached suction and pressure side boundary layers where the location of transition moves upstream with increasing Reynolds number. This dependence is characterized by a minima (maxima) near $Re_C = 4 \times 10^6$ in the variation with Re_C of the suction (pressure) side boundary-layer momentum thickness. This distinguishes $Re_C = 4 \times 10^6$ as the test condition with the greatest symmetry between the suction and pressure side boundary layers. The characteristics of these boundary layers set the initial conditions for the wake development. This is particularly true in the outer part of the near wake where boundary-layer properties persist beyond separation.

Secondly, much of the trailing-edge geometry dependence of the mean flow is a mere displacement of suction side boundary-layer flow over the blunter trailing edge having the larger bevel angle (geometry II). Here, boundary-layer separation is moved aft compared to that on the thinner trailing edge (geometry I), but the thicker trailing edge leads to a thicker near wake. In addition, when combined with prior flat-plate measurements, the observed trends in turbulent boundary-layer separation location show that the shape-factor at separation is lower on more highly curved surfaces.

Thirdly, when the separated boundary layers pass the trailing edge and merge to form the foil's wake, they relax quickly with downstream distance to conform to classical wake scaling laws. However, the manner in which the wake develops depends on its initial thickness and symmetry. The most symmetric wake profile was found at $Re_C = 4 \times 10^6$ for both trailing edges. These flows are distinguished by the thin suction side boundary layers and thick pressure side boundary layers near the trailing edge that create the most symmetrical near wakes found in these studies. The most symmetrical near wake ($Re_C = 4 \times 10^6$, geometry II) thickens the most rapidly. Fluctuating flow-field results (not presented here) suggest near-wake vortex shedding occurs to some degree for both trailing edges at $Re_C = 4 \times 10^6$, and that this phenomenon drives the mean-flow development.

Thus, the final conclusion can be stated: the mechanism by which the initial wake profile shape, thickness and symmetry determine the subsequent wake evolution is likely to be found in the flow's dynamic components.

The authors of this paper wish to the acknowledge the contributions of Shiyao Bian and Kent Pruss of the University of Michigan; William Blake, Michael Cutbirth, Ken Edens, Bob Etter, Ted Farabee, Jon Gershfeld, Joe Gorski, Tom Mathews, David

Schwartzenberg, Jim Valentine, Phil Yarnall, Joel Park, and the LCC technical staff from the Naval Surface Warfare Center – Carderock Division; and Pat Purtell and Candace Wark from the Office of Naval Research. In addition, the authors wish to thank the Office of Naval Research for supporting this research effort under contract numbers N00014-99-1-0341 and N00014-99-1-0856.

REFERENCES

Bastedo, W. G. & Mueller, T. J. 1986 Spanwise variation of laminar separation bubbles on wings at low Reynolds numbers. *AIAA J. Aircraft* **23**, 687–694.

Bearman, P. W. 1965 Investigation of the flow behind a two-dimensional model with a blunt trailing edge fitted with splitter plates. *J. Fluid Mech.* **21**, 241–255.

Benedict, R. P. 1984 *Fundamentals of Temperature, Pressure, and Flow Measurements*, pp. 340–349. Wiley.

Blake, W. K. 1975 A statistical description of the pressure and velocity fields at the trailing edges of flat struts. *David Taylor Naval Ship Research and Development Center Rep.* 4241, Bethesda, Maryland.

Blake, W. K. 1986 *Mechanics of Flow Induced Sound and Vibration*, vol. 2, chap. 11. Academic.

Blake, W. K. & Gershfeld, J. L. 1989 Aeroacoustics of trailing edges. In *Frontiers in Fluid Mechanics* (ed. M. Gad-el-Hak), pp. 457–532. Springer.

Bourgoyne, D. A., Ceccio, S. L., Dowling, D. R., Jessup, S., Park, J., Brewer, W. & Pankajakshan, R. 2001*a* Hydrofoil turbulent boundary layer separation at high Reynolds numbers. *Proc. 23rd Symp. on Naval Hydrodyn. Val de Reuil, France.*

Bourgoyne, D. A., Hamel, J. M., Judge, C. Q., Ceccio, S. L., Dowling, D. R. & Cutbirth, J. M. 2002 Hydrofoil near-wake structure and dynamics at high Reynolds number. *Proc. 24th Symp. on Naval Hydrodyn. Fukuoka, Japan.*

Bourgoyne, D. A., Judge, C. Q., Hamel, J. M., Ceccio, S. L. & Dowling, D. R. 2001*b* Lifting surface flow, pressure, and vibration at high Reynolds number. *Proc. ASME Intl Mech. Engng Conf. and Exposition.*

Brodeur, R. R. & van Dam, C. P. 2000 Transition prediction for a two dimensional Navier–Stokes solver applied to wind-turbine airfoils. *AIAA Paper* 2000-0047.

Covert, E. E. & Lorber, P. F. 1982 Unsteady turbulent boundary layers in adverse pressure gradients. *AIAA Paper* 82-0966.

DeGraaff, D. B. & Eaton, J. K. 2000 Reynolds-number scaling of the flat-plate turbulent boundary layer. *J. Fluid Mech.* **422**, 319–346.

Deutsch, S. & Zierke, W. C. 1987 The measurement of boundary layers on a compressor blade in cascade: Part 1. A unique experimental facility. *Trans. ASME J. Turbomachinery* **109**, 520–526.

Deutsch, S. & Zierke, W. C. 1988*a* The measurement of boundary layers on a compressor blade in cascade: Part 2. Suction surface boundary layers. *Trans. ASME J. Turbomachinery* **110**, 138–145.

Deutsch, S. & Zierke, W. C. 1988*b* The measurement of boundary layers on a compressor blade in cascade: Part 3. Pressure surface boundary layers and the near wake. *Trans. ASME J. Turbomachinery* **110**, 146–152.

Etter, R. J. & Wilson, M. B. 1992 The large cavitation channel. *Proc. 23rd Am. Towing Tank Conf.* New Orleans.

Fitzgerald, E. J. & Mueller, T. J. 1990 Measurements in a separation bubble on an airfoil using laser velocimetry. *AIAA J.* **28**, 584–592.

Fourguette, D., Modarass, D., Taugwalder, F., Wilson, D., Koochesfahani, M. & Gharib, M. 2001 Miniature and MOEMS flow sensors. *AIAA Paper* 2001-2982.

Halstead, D. E., Wisler, D. C., Okiishi, T. H., Walker, G. J., Hodson, H. P. & Shin, H.-W. 1997*a* Boundary layer development in axial compressors and turbines: Part 1 of 4. Composite picture. *Trans. ASME J. Turbomachinery* **119**, 114–127.

Halstead, D. E., Wisler, D. C., Okiishi, T. H., Walker, G. J., Hodson, H. P. & Shin, H.-W. 1997*b* Boundary layer development in axial compressors and turbines: Part 4 of 4. Computations and analyses. *Trans. ASME J. Turbomachinery* **119**, 128–139.

Ho, Y.-H. & Lakshminarayana, B. 1997 Computation of unsteady flow field over a hydrofoil, including boundary layer and wake. *AIAA J.* **35**, 40–50.

Howe, M. S. 1998 *Acoustics of Fluid-Structure Interactions*, Chap. 3. Cambridge University Press.

Kerwin, J. S. 1986 Marine propellers. *Annu. Rev. Fluid Mech.* **18**, 367–403.

Lurie, E. A., Keenan, D. P. & Kerwin, J. E. 1998 Experimental study of an unsteady separating boundary layer. *AIAA J.* **36**, 565–570.

Malick, M. R. 1997 Boundary layer transition prediction toolkit. *AIAA Paper* 97-1904.

Michel, R. 1952 Etude de la transition sur les profils d'aile-establissment d'un point de transition et calcul de la trainée de la profil incompressible. *ONERA Rep.* 1/1578A.

Morris, S. C. & Foss, J. 2001 Turbulent boundary layer to single stream shear layer. *Bull. Am. Phys. Soc.* **46**, 134.

Österlund, J. M., Johansson, A. V., Nagib, H. M. & Hites, M. H. 2000 A note on the overlap region in turbulent boundary layers. *Phys. Fluids* **12**, 1–4.

Schlichting, H. 1979 *Boundary-Layer Theory*, 7th edn, pp. 643, 674–675. McGraw-Hill.

Simpson, R. L. 1989 Turbulent boundary-layer separation. *Annu. Rev. Fluid Mech.* **21**, 205–234.

Sreenivasan, K. R. & Narasimha, R. 1982 Equilibrium parameters for two dimensional turbulent wakes. *Trans ASME* I *J. Fluids Engng* **104**, 167–170.

Thompson, B. E. & Whitelaw, J. H. 1985 Characteristics of a trailing-edge flow with turbulent boundary-layer separation. *J. Fluid Mech.* **157**, 305–326.

Ubaldi, M., Zunino, P., Campora, U. & Ghiglione, A. 1996 Detailed velocity and turbulence measurements of the profile boundary layer in a large scale turbine cascade. *ASME Intl Gas Turbine & Aerospace Congress and Exposition, Birmingham, UK*, paper 96-GT-42.

Volino, R. J. & Hultgren, L. S. 2000 Measurements in separated and transitional boundary layers under low-pressure turbine airfoil conditions. *ASME Intl Gas Turbine & Aerospace Congress and Exposition, Munich, Germany*, paper 2000-GT-260.

Wang, M. & Moin, P. 2000 Computation of trailing-edge flow and noise using large-eddy simulation. *AIAA J.* **38**, 2201–2209.

Wang, M. & Moin, P. 2002 Dynamic wall modeling for large-eddy simulation of complex turbulent flows. *Phys. Fluids* **14**, 2043–2051.

White, F. M. 1991 *Viscous Fluid Flow*, 2nd edn, pp. 268–273, 377, 419, 450–456. McGraw-Hill.